

Pseudo-Spectral Collocation Methods for Hyperbolic Equations with Arbitrary Precision: Applications to Relativistic Gravitation

Daniel Santos-Oliván^{a,b}, Carlos F. Sopena^{a,b}

^a*Institut de Ciències de l'Espai (ICE, CSIC), Campus UAB, Carrer de Can Magrans s/n, 08193 Cerdanyola del Vallès, Spain*

^b*Institut d'Estudis Espacials de Catalunya (IEEC), Edifici Nexus I, Carrer del Gran Capità 2-4, despatx 201, 08034 Barcelona, Spain*

Abstract

Numerical precision is a fundamental aspect of problems in computational physics with high accuracy requirements. The implementation of arbitrary-precision floating-point arithmetics, that can go beyond the usual 64 floating-point arithmetic, is useful whenever it can be applied to numerical algorithms that perform satisfactorily within the significant range of the number of digits of precision. In this paper, we advocate the use of Pseudo-Spectral Collocation methods for implementing high-order bit precision algorithms because of their exponential convergence (for smooth problems) and capacity for high-compression storage of the information. We illustrate the potential of these methods by applying them to very demanding evolution problems in the context of relativistic gravitation. In particular, to problems involving gravitational collapse, whose dynamics exhibits self-similarity properties.

Keywords: Hyperbolic problems, Pseudospectral Methods, Arbitrary-precision arithmetic, Numerical Relativity, Gravitational Collapse.

1. Introduction

The modelling of physical phenomena requires choosing the appropriate type of numerical algorithm that ensures a satisfactory answer in terms of accuracy and reliability but also in terms of efficiency and computational cost. For many scientific problems, it seems reasonable to think that 64-bit (double precision) floating point arithmetics, roughly fifteen or sixteen significant digits, is enough to obtain accurate results. In some cases, even 32-bit (single precision) floating point arithmetics, seven or eight significant figures, can be sufficient. However, there are problems that demand a very high degree of precision [1]. For instance, in systems where long-term solutions strongly depend on the initial conditions or where the physical properties are very sensitive to the value of the parameters, the ability to increase the precision of the numerics is going to be very important.

Finite differences provide simple and easy to work algorithms and finite elements are in general more robust and modular, which is the reason why they are deeply used in engineering problems. Nevertheless, if the priority is to achieve high accuracy then, spectral and pseudospectral methods are a convenient choice due to their great convergence properties (they converge exponentially for smooth problems). It has been shown that they provide precise solutions in a variety of problems, from fluid dynamics to the computation of gravitational-wave templates (see, e.g. [2, 3, 4, 5]). In this paper, we show that the powerful convergence properties of pseudospectral collocation (PSC) methods make them an ideal option to go beyond the typical 64-bit floating-point arithmetics. For this precision, maximum accuracy is usually reached with a relatively quite low number of collocation (discretization) points. Therefore, going beyond of this precision does not constitute a high increase in computational cost. In addition, pseudospectral collocation methods provide a high-compression of the information related to the solution of our problem. Indeed, the number of collocation points (or modes in the spectral picture) needed to reach very high accuracy is much smaller than the number of points in other methods (e.g., finite differences) so that the memory demands reduce drastically.

*Corresponding author

Email address: santos@ice.cat (Daniel Santos-Oliván)

In order to show all these claims, we have developed a new numerical library, **ANETO** (Arbitrary precision solvEr with pseudo-specTral MethOds) [6], which gives us complete flexibility in the numerical precision that we can use in our numerical computations. In other words, we have the possibility to adjust the bit precision of our algorithms to fulfil the exact accuracy requirements of a given problem and also we have a tool to translate numerical codes from the standard double precision to arbitrary precision. The work presented in this paper originates from the experience of the authors in dealing with physical problems in relativistic gravitation, in particular the description of gravitational collapse in several scenarios where gravity is well described by General Relativity (see [7, 8]), that involved finding numerical solutions with high demands in accuracy. We have used the **ANETO** library to solve these Numerical Relativity (the solution of the equations of General Relativity with numerical methods) problems in spherical symmetry. Nevertheless, the conclusions of this paper can be easily extrapolated to different one-dimensional problems or evolution problems, with one space dimension, in other research areas.

The plan of this paper is as follows: In Sec. 2 we briefly review the basic mathematical foundations of the PSC method. In Sec. 3, we show the performance of PSC methods in terms of accuracy and speed for arbitrary precision computations and compare it to the usual floating point arithmetics and also to other popular discretisation methods. We also discuss how parallel computing needs to be included in a practical implementation in order to use high-precision in realistic/complex simulations. In Sec. 4, we describe two examples of full evolution problems in the field of General Relativity that show how we can reach accuracies that are very difficult to obtain using double precision. In Appendix A we describe briefly the basic features of the **ANETO** library.

2. Elements of the PSC method

The method of mean weighted residuals (MWRs) is a set of techniques that allows us to solve differential equations using a basis of functions to approximate the solution. Depending on the choice of basis functions and on the way we impose the expansion in basis functions to “approximate” the solution of the problem we obtain different types of numerical algorithms. This includes finite element methods, PSC methods, etc. More precisely, let us consider a general system of partial differential equations (PDEs) defined over a spatial domain $\mathcal{D} \in \mathbb{R}^d$, being d the number of space dimensions, and for a time interval $t \in [t_i, t_f]$:

$$L[\vec{u}](t, \vec{x}) = 0 \quad (t \in [t_i, t_f], \vec{x} \in \mathbb{R}^d), \quad (1)$$

where $L[\cdot]$ is a given differential operator that determines the form of the PDEs and $\vec{u}(t, \vec{x}) = (u^1(t, \vec{x}), \dots, u^N(t, \vec{x}))$ is the vector of unknowns (N in total). In order to have a well-posed evolution problem, Eq. (1) has to be complemented with boundary and initial conditions. For the purposes of this work, it will be enough to consider the case of just one spatial dimension, i.e. $d = 1$.

The procedure to impose that a given set of unknowns \vec{u}_N is an approximate solution to Eq. (1) is the following: First, let us consider a set of test functions, $\{\Psi_j(x)\}_{j=0, \dots, N_{bf}}$. Then, we impose the following set of conditions:

$$\int_{\mathcal{D}} dx \Psi_j(x) L[\vec{u}](t, x) = 0 \quad (j = 0, \dots, N_{bf}). \quad (2)$$

It is precisely the form of the test functions (in the broad sense, i.e. including distributions) that determines the particular characteristics of the specific MRW method we adopt to approximate the solutions to this set of PDEs. The next step is to use the expansion of our approximate solutions \vec{u}_N to the system of PDEs in terms of the basis of functions mentioned above:

$$\vec{u}_N(t, x) = \sum_{k=0}^N \vec{a}_k(t) \phi_k(x), \quad (3)$$

where ϕ_k are the basis functions and \vec{a}_k are the (spectral) coefficients of this expansion. This expansion would be exact if we allow for an infinite number of terms ($N \rightarrow \infty$), but since we are looking for an approximation, we just take a truncate finite version. The error in adopting the approximation in Eq. (3) decreases as we increase the number of terms considered in the expansion, i.e. N . In general, when $N_{bf} = N$, the result of introducing the approximation in Eq. (3) into the set of conditions in Eq. (2) is a set of Ordinary Differential Equations (ODEs) for the $N + 1$ time-dependent spectral coefficients contained in the vector $\vec{a}_k(t)$ that we can solve using the well-known **Method of**

Lines (see, e.g. [9]). A particular type of MRW is the one that leads to the PSC method (see, e.g. [10, 11, 12]). The test “functions” corresponding to this case are the Dirac delta distributions associated with the particular choice of collocation points, $\{x_j\}_{j=0,\dots,N}$, that we want to use for the PSC method:

$$\Psi_j(x) = \delta(x - x_j) \quad (j = 0, \dots, N). \quad (4)$$

The choice of these functions in Eq. (2) imposes the condition that the set of PDEs in Eq. (1) has to be fulfilled exactly at all the collocation points $\{x_j\}_{j=0,\dots,N}$. This is precisely what characterizes the PSC methods among the spectral methods. The most convenient choice of the basis functions in Eq. (3) depends on the particular features of the problem under consideration. For instance, Fourier series are naturally adapted to problems with periodic boundary conditions and spherical harmonics are specially suitable when we are using spherical coordinates. In a general case, in a one-dimensional problem, the a priori best choice are Chebyshev polynomials,

$$T_n(X) = \cos(n \cos^{-1}(X)) \quad (X \in [-1, 1]). \quad (5)$$

The main reason to support this choice is the Cauchy interpolation error theorem and the Chebyshev minimal amplitude theorem [11], which tell us that the optimal location of interpolation points for N collocation points is given by the roots of the Chebyshev polynomial of order $N + 1$. There are several possible choices of Chebyshev roots that fulfil this condition. The one we are considering here is the set of *Lobatto-Chebyshev* collocation points. The key feature of the Lobatto-Chebyshev grid is that it includes the boundary points $X = \pm 1$ and hence we can impose the boundary conditions directly on these points. The Lobatto-Chebyshev collocation points are given by the roots of the following equation:

$$(1 - X^2) T'_N(X) = 0, \quad (6)$$

where the prime denotes differentiation with respect to X . The roots of this equation can be written down explicitly as:

$$X_i = -\cos\left(\frac{\pi i}{N}\right) \quad (i = 0, 1, \dots, N). \quad (7)$$

Then, with the choice of basis functions, $\phi_k(x) = T_k(X)$ ¹, and the choice of collocation points in Eq. (7), we have now two representations of the approximation to the solution [Eq. (3)] of our system of PDEs [Eq. (1)]. The first representation is the spectral one, which comes directly from Eq. (3), that is:

$$\vec{u}_N(t, x) = \sum_{n=0}^N \vec{a}_n(t) T_n(X), \quad (8)$$

where a mapping between the physical coordinate x and the spectral one X , $x = x(X)$ is assumed. The time-dependent vector $\vec{a}_n(t) = (a^1(t), \dots, a^N(t))$ (we recall that N is the number of unknowns) contains the spectral coefficients of the pseudospectral approximation to our variables \vec{u} . In this representation, the order of magnitude of the spectral coefficients decays exponentially with the degree n of the Chebyshev polynomial:

$$|a_n^k| \sim e^{-\alpha^k n} \quad (k = 1, \dots, N; n = 0, \dots, N), \quad (9)$$

where α^k is a coefficients associated with the variable u^k . As a consequence, the discretization error due to the use of a finite number of points also decays exponentially. This behaviour is illustrated in Figure 1 for numerical computations using different number of digits of precision. The other type of representation that we have in the case of the PSC method is the one sometimes called *physical* representation, which looks as follows:

$$\vec{u}_N(t, x) = \sum_{i=0}^N \vec{u}_i(t) C_i(X), \quad (10)$$

¹In general, the coordinates x and X will be different and an invertible mapping between the physical domain of the coordinate x and the spectral domain of the spectral one ($X \in [-1, 1]$), $x = x(X)$, needs to be provided as discussed later in this section.

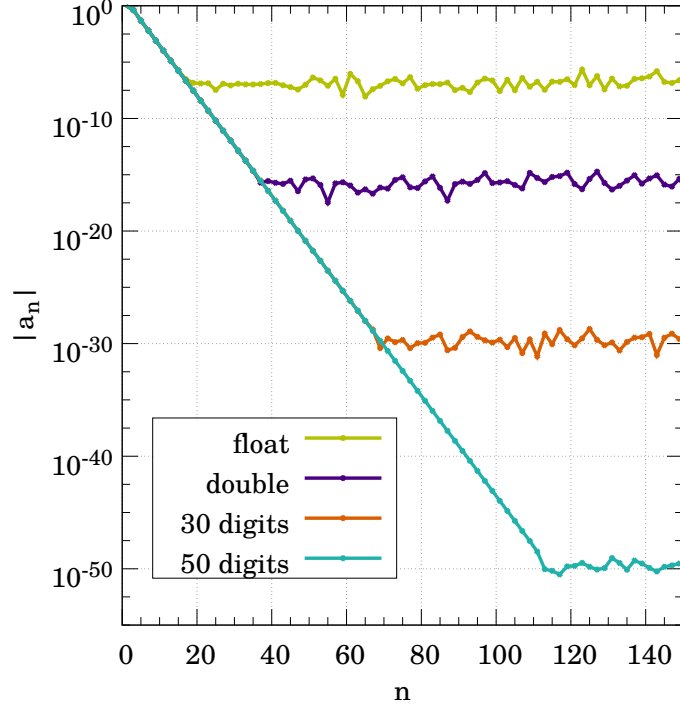


Figure 1: **Representation of the Spectral Coefficients.** For a smooth enough function, the modes in the spectral representation decay exponentially until they reach the precision error of our computations. With the use of arbitrary precision, more number of digits, we can control this error.

where again a mapping between the physical coordinate x and the spectral one X , $x = x(X)$, is assumed and where $\vec{u}_i(t)$ are the values of our variables \vec{u} at the collocation point X_i , and $\{C_j(X)\}_{j=0,\dots,N}$ are the *cardinal functions* [11] associated with our choice of basis functions and set of collocation points, which obey the set of relations: $C_i(X_j) = \delta_{ij}$ ($\forall i, j = 0, \dots, N$). In the case of the Lobatto-Chebyshev collocation grid, the cardinal functions can be written down as

$$C_i(X) = \frac{(1 - X^2)T'_N(X)}{(1 - X_i^2)(X - X_i)T''_N(X_i)} \quad (i = 0, \dots, N). \quad (11)$$

These two types of representation of the approximation for the unknowns, the spectral one in Eq. (8) and the physical one in Eq. (10) are related via a matrix transformation. Given the spectral coefficients, a_n ($n = 0, \dots, N$), of a certain function u we can obtain the collocation values, u_i ($i = 0, \dots, N$), by just introducing the values of the collocation points in Eq. (8), so that we can write the matrix transformation:

$$u_i = \sum_{n=0}^N M_{in} a_n, \quad M_{in} = T_n(X_i) \quad (i, n = 0, \dots, N), \quad (12)$$

and the inverse transformation can be derived from the physical representation of Eq. (10) assuming that the basis functions are orthogonal polynomials coming from a Sturm-Liouville problem and the quadrature properties associated with the zeros (the collocation grid) of these polynomials. Then, apart from the orthogonality properties of these polynomials in the continuum they also have a discrete scalar product associated with the collocation grid [11]:

$$[T_n, T_m] = \sum_{i=0}^N w_i T_n(X_i) T_m(X_i) = \delta_{nm} v_n^2, \quad (13)$$

where w_i are the weights and the constants v_n^2 determine the norm of the orthogonal polynomials. This is essentially the well-known integration formula based on Gaussian quadratures. In the case of Chebyshev polynomials and a Lobatto-Chebyshev collocation grid we have that $w_i = \pi/(N\bar{c}_i)$, with $\bar{c}_n = 2$ if $n = 0$ or $n = N$ and $\bar{c}_n = 1$ otherwise. Then, using these definitions we have that $v_n^2 = \pi\bar{c}_n/2$. As we can see, the Chebyshev polynomials are orthogonal in this scalar product associated to the particular collocation grid. Using this property, the spectral coefficients \vec{d}_n , using Eq. (8), can be written as:

$$\vec{d}_n = \frac{[\vec{u}_N, T_m]}{[T_n, T_n]} = \frac{[\vec{u}_N, T_m]}{v_n^2} = \frac{1}{v_n^2} \sum_{i=0}^N w_i u_i T_n(X_i), \quad (14)$$

from where we can extract the components of the inverse matrix transformation between representations:

$$\mathbb{M}_{ni}^{-1} = \frac{T_n(X_i)w_i}{v_n^2}. \quad (15)$$

It is clear that the cost of the computations to carry out any of these transformations increases quadratically with the number of collocation points, i.e. as $\sim N^2$. However, in the case of Chebyshev PSC methods there is an extra property that changes this. Indeed, we can introduce the following new coordinate associated with the spectral coordinate X :

$$X = \cos \theta \quad (\theta \in [0, \pi]), \quad (16)$$

so that the series in Chebyshev polynomials [Eq. (5)] becomes a cosine series since $T_n(\cos \theta) = \cos(n\theta)$. In the particular case of the Lobatto-Chebyshev collocation grid, the components of the matrix transformation in Eq. (12) can be written in the following form: $\mathbb{M}_{in} = T_n(X_i) = (-1)^n \cos(n i \pi/N)$. The resulting transformation becomes then a Discrete Cosine Transform (DCT). This is very useful because this transformation can be computed by using a $2N$ Fast Fourier Transform (FFT) algorithm. With this we can decrease the number of computations so that the actual cost of the transformation scales as $\sim N \ln N$ with the number of collocation points [10, 11].

Coming back to the form of the approximation $\vec{u}_N(t, x)$ to the exact solution $\vec{u}(t, x)$, we have already mentioned that one needs to specify a mapping between the *physical* spatial coordinate x and the spectral coordinate X , which in the case of the Chebyshev polynomials is in the range: $X \in [-1, +1]$. Let us assume that the *physical* coordinate x takes values in the interval $\Omega = [x_L, x_R]$. Then, one of the most common mappings used in the literature is the simplest one, the linear mapping:

$$X \longrightarrow x(X) = \frac{x_R - x_L}{2} X + \frac{x_L + x_R}{2}, \quad (17)$$

where x_L and x_R are the boundary points of the physical domain. Obviously, the distribution (density) of the grid points in x is the same as the distribution of collocation points in X . However, there are situations where it is more convenient to use a non-trivial mapping. For instance, in evolutionary problems, like the ones we are interested in this paper, the fact that the Chebyshev collocation points are accumulated near the boundaries [according to Eq. (7)] puts stringent constraints on the Courant-Friedrichs-Lewy (CFL) condition for the stability of the evolution of the PDEs (see, e.g. [13]). In the case of the PSC method, the CFL condition takes the form $\Delta t < C N^{-2}$ (where C is a certain constant), in contrast with the typical form for standard finite-difference schemes for PDEs, where $\Delta t < C' N^{-1}$ (where C' is another constant). We can use the mapping $x(X)$ to change the distribution of points in the physical space and improve the CFL condition. Another application of the adaptation of this mapping is mesh refinement, that is, to distribute the points around the regions where more resolution is needed. Nevertheless, from a general perspective, any reasonable mapping can be used as long as it is smooth enough and has a non-vanishing derivative in the coordinate range considered [14]. We give here two more examples of mappings that can be used. First, one that mimics a uniform grid in x :

$$X \longrightarrow x(X) = \gamma + \beta \frac{\arcsin(\alpha X)}{\arcsin(\alpha)}, \quad (18)$$

where the uniformity in the separation of the points is controlled by the parameter α . Setting it to one makes the grid exactly uniform but singular. This can be avoided by taking $\alpha = 1 - \epsilon$ with ϵ very small. This reproduces an almost uniform grid without any singularity. By setting this parameter to zero, we recover the Lobatto-Chebyshev grid. The

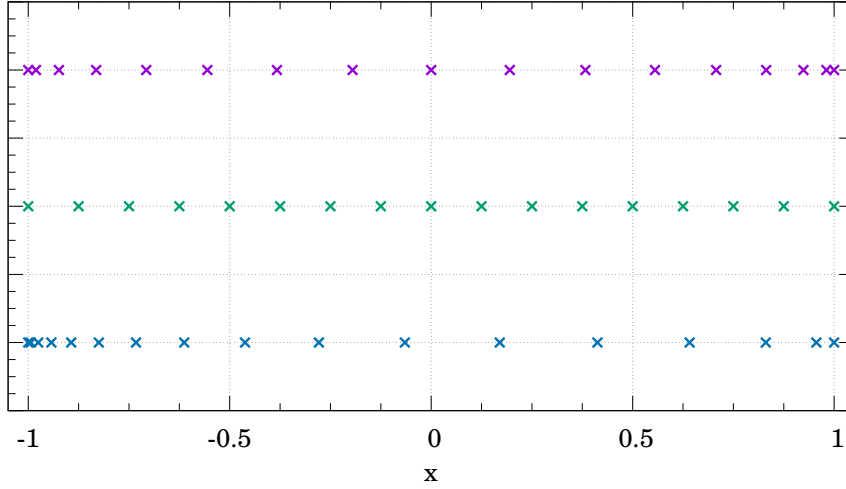


Figure 2: **Mappings between the Physical and Spectral Grids.** The upper (purple) points show the distribution of points in an usual Lobatto-Chebyshev grid, Eqs. (7) and (17). The middle (green) ones represent a uniform mapping as defined in Eq. (18) with $\alpha = 1$. In the bottom (blue), the distributions of points corresponds to Eq. (19) with $\alpha = 1$.

range of the coordinate x can be controlled with the constants β and γ . This mapping was introduced by Kosloff and Tal-Ezer [15] in order to recover a CFL condition of the type $\Delta t \sim O(N^{-1})$. The second example that we present is a mapping that accumulates grid points near only one of the two boundaries. It is based on a simple exponential function:

$$X \longrightarrow x(X) = \gamma + \beta e^{\alpha(1+X)}, \quad (19)$$

where, again, β and γ determine the range of the coordinate x and α controls how strong is the accumulation of grid points. In this example the grid points are accumulated near the left boundary of x . A graphical representation of the three mappings in Eqs. (17), (18) and (19) is shown in Figure 2.

Apart from the Cauchy interpolation error theorem and the possibility of using the FFT algorithm for the change between the physical and spectral representations, there is another very important advantage of using the PSC method. This advantage is of particular relevance for the solution of time-dependent problems described by PDEs. Indeed, the PSC method provides the physical representation of the approximation to our variables. Then, instead of using the spectral coefficients, $\vec{a}_n(t)$, we can take the collocation values of our variables, $\vec{u}_i(t)$, as the unknowns to be found as the solution of our PDEs. This is particularly useful when we have to deal with non-linear terms, like for instance $u^2 \equiv \vec{u} \cdot \vec{u}$, since the collocation values of this quantity are simply $u_i^2 = \vec{u}_i \cdot \vec{u}_i$. In the spectral picture, the spectral coefficients of u^2 are given as a double sum. In general, for any function of \vec{u} , say $\vec{f}(\vec{u})$, the collocation values can be immediately found as: $\vec{f}(\vec{u})_i = \vec{f}(\vec{u}_i)$. Therefore, nonlinear terms in the PDEs can be dealt in a simple and natural way with the PSC method.

In a similar way, the change between the physical and spectral representations allows us to deal with more complex operators than an arithmetic function, in particular with differentiation and integration. In the case of derivatives, the computation can be fully performed in the physical representation by using a matrix multiplication that involves all the values of our function in the collocation grid. Indeed, from Eq. (10)

$$\frac{\partial \vec{u}}{\partial x} = \sum_{i=0}^N \vec{u}_i(t) \frac{dX(x)}{dx} \frac{dC_i(X)}{dX} \implies (\partial_x \vec{u})_k = \sum_{i=0}^N \vec{u}_i(t) \left(\frac{dX(x)}{dx} \right)_{X=X_k} \left(\frac{dC_i(X)}{dX} \right)_{X=X_k}, \quad (20)$$

or in matrix form

$$(\partial_x \vec{u})_i = \sum_{k=0}^N C_{ik} \vec{u}_k, \quad C_{ik} = \left(\frac{dX(x)}{dx} \right)_{X=X_k} \left(\frac{dC_i(X)}{dX} \right)_{X=X_k} \quad (i, k = 0, \dots, N). \quad (21)$$

An alternative way of carrying out the computation of $(\partial_x \vec{u})_i$ is to transform to the spectral space where the differentiation operation is much simpler, involving just linear operations on the spectral coefficients. Indeed, for Chebyshev expansions the spectral coefficients of the derivatives \vec{b}_n of variables with spectral coefficients \vec{a}_n are given by the well-known algorithm [11, 10]:

$$\begin{cases} \vec{b}_N = 0, \\ \vec{b}_{N-1} = 2N\vec{a}_N, \\ \vec{b}_n = \frac{1}{\bar{c}_n} [2(n+1)\vec{a}_{n+1} + \vec{b}_{n+2}] \quad (n = N-2 \dots 0), \end{cases} \quad (22)$$

where we recall that $\bar{c}_n = 2$ if $n = 0$ and $\bar{c}_n = 1$ otherwise. Then, the scheme for the computation of derivatives in the Chebyshev PSC method is as follows:

$$\partial_x : \{\vec{u}_i\} \xrightarrow{DCT} \{\vec{a}_n\} \xrightarrow{\tilde{\partial}_x} \{\vec{b}_n\} \xrightarrow{DCT} \{(\partial_x \vec{u})_i\}, \quad (23)$$

where $\tilde{\partial}_x$ is the derivative operator in the spectral space whose action is given in Eq. (22). Assuming that the transformation between representations is done through a DCT transformation, the cost of a derivative scales as $N \log N$.

In the case of integration, there are different operators that are of interest depending on the problem/computation we are dealing with. For instance, in the case of a simple first-order linear ODE, we can always rewrite it so that the solution is obtained from direct integration. For instance, let us consider

$$\frac{df(x)}{dx} = g(x), \quad (24)$$

with a boundary condition at $x = x_0$. The solution is simply given by

$$f(x) = f(x_0) + \int_{x_0}^x dx' g(x'). \quad (25)$$

To carry out this type of integrals we implement a generic integration scheme that we call *integration from the left* because it incorporates a (boundary) condition at $X = X_- = -1$ (where we are assuming there is a mapping between the spectral and physical coordinates, $x = x(X)$, so that the point x_0 is mapped to X_- , i.e. $x(-1) = x_0$):

$$I_L(x(X)) = I_L(x_0) + \int_{X_-}^X dX' \left(\frac{dx}{dX} \right)_{X'} g(X'), \quad (26)$$

where $I_L(x_0) = f(x_0)$. In practice, this computation can be carried out with a scheme similar to the one for the case of derivatives [Eq. (23)]. For our vector of variables, \vec{u} , the full left-integration process is:

$$\int_{X_-}^X : \{\vec{u}_i\} \xrightarrow{DCT} \{\vec{a}_n\} \xrightarrow{\int_L} \{\vec{b}_n^L\} \xrightarrow{DCT} \{(\int_{X_-}^X \vec{u})_i\}, \quad (27)$$

where $\{\vec{b}_n^L\}$ are the spectral coefficients associated with the integral $I_L(x(X))$, and their relation to the spectral coefficients of the variables \vec{u} , $\{\vec{a}_n\}$, the operation denoted by \int_L in Eq. (27), are given by:

$$\begin{cases} \vec{b}_N^L = \frac{\vec{a}_{N-1}}{2N}, \\ \vec{b}_n^L = \frac{1}{2n} (\bar{c}_{n-1} \vec{a}_{n-1} - \vec{a}_{n+1}) \quad (n = N-1, \dots, 1), \\ \vec{b}_0^L = I(x(X_-)) - \sum_{n=1}^N (-1)^n \vec{b}_n. \end{cases} \quad (28)$$

In the same way, we can introduce the integration with a boundary condition imposed at the right boundary, i.e. at $X = X_+ = +1$:

$$I_{\mathbb{R}}(x(X)) = I_{\mathbb{R}}(x_0) + \int_X^{X_+} dX' \left(\frac{dx}{dX} \right)_{X'} g(X'). \quad (29)$$

The process is totally equivalent to the one in Eq. (27), that is:

$$\int_X^{X_+} : \{\vec{u}_i\} \xrightarrow{DCT} \{\vec{a}_n\} \xrightarrow{\int_{\mathbb{R}}} \{\vec{b}_n^{\mathbb{R}}\} \xrightarrow{DCT} \{(\int_X^{X_+} \vec{u}_i)\}. \quad (30)$$

We just need to specify the action of the operator $\int_{\mathbb{R}}$ on the spectral, i.e. on the spectral coefficients of our variables, $\{\vec{a}_n\}$,

$$\begin{cases} \vec{b}_N^{\mathbb{R}} = -\frac{1}{2N} \vec{a}_{N-1}, \\ \vec{b}_n^{\mathbb{R}} = -\frac{1}{2n} (c_{n-1} \vec{a}_{n-1} - \vec{a}_{n+1}) & (n = N-1, \dots, 1), \\ \vec{b}_0^{\mathbb{R}} = I_{\mathbb{R}}(x(X_+)) - \sum_{n=1}^N \vec{b}_n^{\mathbb{R}}. \end{cases} \quad (31)$$

Apart from solving trivial ODEs, this method can also be used for problems involving more complex ODEs, in particular for those that originate from the spatial discretization, using the PSC method, of evolution systems governed by PDEs. Moreover, ODEs can appear in evolution problems as constraints equations. The resulting ODEs can be discretised using PSC methods. This will lead, in general, to a linear system that we need to solve. As an example, let us consider the following second-order linear ODE:

$$\alpha_2(X) \frac{d^2 f(X)}{dX^2} + \alpha_1(X) \frac{df(X)}{dX} + \alpha_0(X) f(X) = S(X). \quad (32)$$

Once it is discretized using the PSC method, the functions of the spectral coordinate X become vectors of the values of the functions at the collocation points and the differential operators become matrices. Then, the linear algebra problem that we have to solve has the form:

$$\sum_{j=0}^N [\vec{a}_2^i \mathcal{D}_{XX}^{ij} + \vec{a}_1^i \mathcal{D}_X^{ij} + \vec{a}_0^i(X) \mathbb{I}^{ij}] \vec{f}^j = \vec{S}^i, \quad (33)$$

where \vec{a}_0 , \vec{a}_1 , \vec{a}_2 , \vec{f} , and \vec{S} represent the $N+1$ vectors of the collocation values of the functions $\alpha_0(X)$, $\alpha_1(X)$, $\alpha_2(X)$, $f(X)$, and $S(X)$ respectively; \mathbb{I} denotes the $(N+1) \times (N+1)$ identity matrix; \mathcal{D}_X^{ij} , the matrix associated with the first-order differential operator d/dX ; and \mathcal{D}_{XX}^{ij} the matrix associated with the second-order one, d^2/dX^2 . In contrast with what happens when using other type of numerical algorithms, the matrix between the square brackets of Eq. (33) is sparse, which means that solving this problem can be computationally quite costly. In practice, given the compression property of the PSC method, mainly due to its exponential convergence, the value of N is generally much smaller than in order numerical methods and then, the computational cost is quite reasonable. In addition, if we use a multidomain decomposition, like the one we discuss in the next section, we will reduce the sparsity of the matrix.

For a general ODE, assuming the highest-order derivative is of order O , we can generalize the form of the linear problem in Eq. (33) to the simple form:

$$\sum_{j=0}^N \mathcal{O}^{ij} \vec{f}^j = \sum_{k=1}^O \sum_{j=0}^N [\vec{a}_k^i \mathcal{D}_{(k)}^{ij}] \vec{f}^j = \vec{S}^i, \quad (34)$$

where we have adopted the following conventions: $\mathcal{D}_{(0)}^{ij} = \mathbb{I}^{ij}$, $\mathcal{D}_{(1)}^{ij} = \mathcal{D}_X^{ij}$, and $\mathcal{D}_{(2)}^{ij} = \mathcal{D}_{XX}^{ij}$, and in general $\mathcal{D}_{(k)}^{ij}$ is the matrix associated with the differential operator d^k/dX^k . The first-order differentiation matrix, $\mathcal{D}_{(1)}^{ij}$, is given by

(see, e.g. [11]):

$$\mathcal{D}_{(1)}^{ij} = \begin{cases} \frac{\bar{c}_i}{\bar{c}_j} \frac{(-1)^{i+j}}{X_i - X_j} & i \neq j, \\ -\frac{X_i}{2(1-X_i^2)} & 1 \leq i = j \leq N-1, \\ \frac{2N^2+1}{6} & i = j = 0, \\ -\frac{2N^2+1}{6} & i = j = N. \end{cases} \quad (35)$$

We can have write down analytical expressions like this one for higher-order differentiation matrices (see, e.g. [16] for the second-order case), but in general they can be obtained from the first-order differentiation matrix as follows:

$$\mathcal{D}_k^{ij} = \left(\mathcal{D}_{(1)}^k \right)^{ij} = \left(\mathcal{D}_{(1)} \times \cdot^k \cdot \mathcal{D}_{(1)} \right)^{ij}. \quad (36)$$

Then, all we have to do is to built the matrix O^{ij} in Eq. (34) and then, to invert the system to obtain the vector of collocation values $f^{\vec{i}}$. In the case of non-linear differential equations, the system cannot be directly inverted and we have to resort to iterative methods.

We end this part by discussing another very useful tool in the PSC method: Filtering. In numerical computations using the PSC method, and in particular in evolution problems, numerical noise usually originates as low-amplitude high-frequency modes that eventually can pile up along the numerical evolution, sometimes making the algorithm unstable and in many cases preventing us to obtain the correct solution to our problem. In the spectral representation, these high-frequency modes are identifiable and we can eliminate them by applying a filter acting on the high-frequency part of the spectrum. The filter has to be carefully chosen in order to avoid eliminating modes that contain part of the solution to our problem, but in general, as Figure 8 shows, these modes are usually at the level of round-off error and we can eliminate them without altering the real content of the solution. For our vector of variables, \vec{u} , the filtering process (with associated filter σ) can be described as follows:

$$\sigma : \{\vec{u}_i\} \xrightarrow{DCT} \{\vec{d}_n\} \xrightarrow{\sigma} \{\vec{d}_n^\sigma\} = \left\{ \sigma \left(\frac{n}{N} \right) \vec{d}_n \right\} \xrightarrow{DCT} \{\vec{u}_i^\sigma\}. \quad (37)$$

A frequently used filter is the exponential filter:

$$\sigma(\eta) = \exp\{-\alpha \eta^\gamma\}, \quad (38)$$

where α and γ are freely specifiable parameters of the filter. The parameter α is usually fixed to $\alpha = -\log \varepsilon_M$, where ε_M represents the machine accuracy ($\alpha \approx 36.0437$ for double precision). The typical values of γ that we have used are of the order of $\sim (9/5)N$.

2.1. The Multidomain PSC Method

Up to this point, we have discussed the PSC method assuming that the whole computational domain would be mapped to a single Lobatto-Chebyshev spectral domain $([-1, 1])$. However, in some applications, the need for high spatial resolution may be restricted to certain regions of the computational domain and hence, the single-domain approach is not very effective. To ensure the efficiency of our computations some form of grid refinement needs to be adopted. Among the different possibilities, in the case of the PSC method, a simple one is to use a multidomain scheme in such a way that each of the subdomains is mapped to a Lobatto-Chebyshev collocation grid so that we can distribute the subdomains to put more of them around the regions where high resolution is required. For the case of evolution problems in one spatial dimension we consider a decomposition of our physical computation domain $\Omega = [x_L, x_R]$ in D disjoint subdomains:

$$\Omega = \bigcup_{a=0}^{D-1} \Omega_a, \quad \Omega_a = [x_{a,L}, x_{a,R}], \quad (39)$$

with the identification: $x_{a,R} = x_{a+1,L}$ ($a = 0, \dots, D-2$). Each subdomain Ω_a is mapped into the spectral domain $[-1, +1]$. For the sake of simplicity, in what follows we assume a linear mapping, but other mappings like the ones

in Eqs. (18) and (19) are also possible. Then, given the coordinate x of a point in the physical domain Ω , assuming it belongs to the subdomain Ω_a , it is mapped to a spectral coordinate X_a according to the following linear mapping:

$$x \longrightarrow X_a(x) = \frac{2x - x_{a,L} - x_{a,R}}{x_{a,R} - x_{a,L}}. \quad (40)$$

The inverse mapping is:

$$X_a \longrightarrow x(X_a) = \frac{x_{a,R} - x_{a,L}}{2} X_a + \frac{x_{a,L} + x_{a,R}}{2}. \quad (41)$$

and the Jacobian of the transformation is simply given by:

$$\frac{dx}{dX_a} = \frac{x_{a,R} - x_{a,L}}{2}. \quad (42)$$

As we can see, the Jacobian is different from subdomain to subdomain unless all of them have the same physical coordinate size. Despite the simplicity of the linear mapping it can be used for refinement adapting the length of each subdomain to the resolution needs of the problem under consideration. All what we need is a refinement criteria for the adaptation of the subdomain sizes.

In order to use a multidomain scheme, we need to adapt the pseudospectral operations described above for single-domain problems. For most of the operations, the generalization to a multidomain scheme is straightforward since the operation can be performed independently subdomain by subdomain, thus we are not going to discuss them here. However, some operations require some extra ingredients in order to work in the multidomain framework. These extra ingredients are related to the communication between subdomains or to boundary problems. The case of differentiation is a good example. In principle, we can perform derivatives in a multidomain scheme by performing the differentiation at each subdomain separately. However, as it is well-known (see also Sec. 3 in this paper), sometimes the computation of the derivative in the PSC method becomes noisy, producing an accumulation of error at the points near the boundaries with respect to the interior ones. Here we can take advantage of the multidomain scheme in order to reduce the error by using a dual grid scheme. The idea is to use a second grid that is constructed in such a way that the boundaries of the subdomains coincide with the middle points of the subdomains of the main (original) grid (see Figure 3). In this way, the dual grid has $D + 1$ subdomains, $\{\bar{\Omega}_{\bar{a}}\}_{\bar{a}=0,\dots,D}$, in such a way that the left boundary location of each subdomain, say \bar{a} ($= 0, \dots, D$), is given by $\bar{x}_{\bar{a},L} = (x_{\bar{a}-1,L} + x_{\bar{a},R})/2$ (excepting for $\bar{a} = 0$, in which case it is simply the global left boundary point x_L), and the right boundary location is given by $\bar{x}_{\bar{a},R} = (x_{\bar{a},L} + x_{\bar{a},R})/2$ (excepting for $\bar{a} = D$, in which case it is simply the global right boundary point x_R). When we compute the derivative in the dual grid, the points where typically the error is the lowest coincide with the location where the error is typically the greatest in the subdomains of the main grid. Then, we compute the final derivative of our function by combining the derivatives computed separately in the main (f'_{main}) and dual (f'_{dual}) grids. For a given point x belonging to the subdomain Ω_a of the main grid, the derivative is the following weighted sum of the derivatives from the main and the dual grids:

$$f'(x) = \pi_a(x) f'_{\text{main}}(x) + (1 - \pi_a(x)) f'_{\text{dual}}(x) \quad (x \in \Omega_a), \quad (43)$$

where $\pi_a(x)$ is a weighting function on the subdomain Ω_a of the main grid (that together with the function $1 - \pi_a(x)$ they form a partition of unit associated with the subdomain Ω_a). This function takes values between zero and one, being zero in the boundaries of the subdomains of the main grid and one at the boundaries of the dual grid that is smooth between the boundary and the centre of the subdomain. One example of a partition function is:

$$\pi_a(x) = \begin{cases} \frac{(x-x_{a,L})(x-x_{a,R})}{(x-x_{a,L})(x-x_{a,R})+(x-\bar{x}_{a,L})(x-\bar{x}_{a,R})} & \text{if } x \in \bar{\Omega}_a, \\ \frac{(x-x_{a,L})(x-x_{a,R})}{(x-x_{a,L})(x-x_{a,R})+(x-\bar{x}_{a+1,L})(x-\bar{x}_{a+1,R})} & \text{if } x \in \bar{\Omega}_{a+1}. \end{cases} \quad (44)$$

This structure of $\pi_a(x)$ is due to the fact that a point of the subdomain Ω_a can either be at the subdomain $\bar{\Omega}_a$ or $\bar{\Omega}_{a+1}$ of the dual grid (see Figure 3).

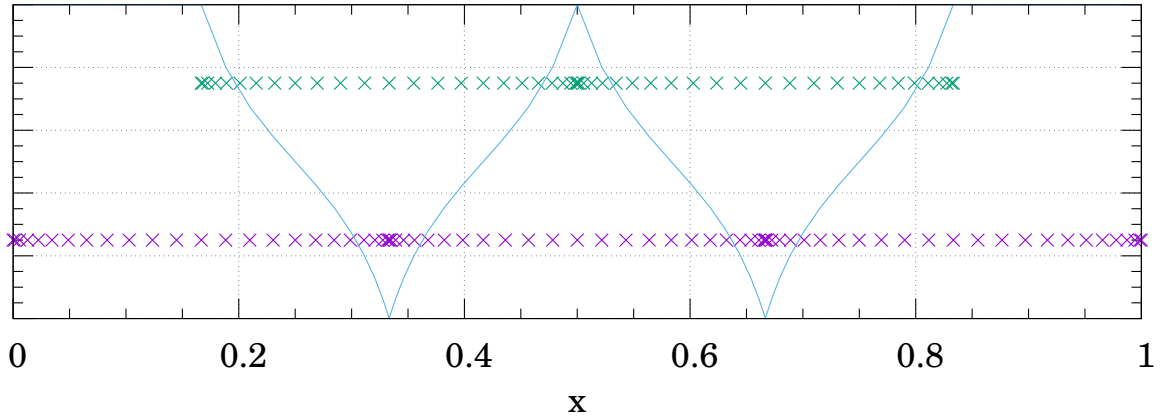


Figure 3: **Structure of a Dual Grid.** Schematic representation that shows the structure of a particular implementation of a dual grid scheme. The main grid (in purple) is composed of three subdomains and the dual grid (in green) is shifted and has four subdomains (one more), but we do not show the subdomains that contain the global boundaries, which require a special treatment, just the two interior subdomains. The blue line shows the weighting function $\pi_a(x)$ of Eq. (44).

Apart from providing a framework for resolution refinement and also facilitating certain operations with the PSC method, the multidomain scheme is also a way of using parallelization in the practical numerical computations. Indeed, apart from the communications across subdomains and special boundary treatments, the largest part of the computations can be carried out independently within the different subdomains (see Sec. 3.4 for more details). This is obvious in the case of operations involving differentiation that we have shown above and where we have seen that the operations at the different subdomains are indeed independent. We are going to show that it is also true for the case of operations involving integration. Looking at the expression for integration in Eq. (26) may give the impression that it is a sequential operation since the result for a certain x_o depends on all the computations required for smaller values, $x < x_o$. Nevertheless, this is not an obstruction to parallelization since we can compute, within each subdomain separately, the following partial integrals associated with a point x belonging to a subdomain Ω_a :

$$I_{L,a}(x) = \int_{x_{a,L}}^x dx' g(x') = \int_{-1}^{X(x)} dX' \left(\frac{dx}{dX} \right)_{X'} g(X'). \quad (45)$$

Then, the full integral can be computed as:

$$I_L(x) = O_a + I_{L,a}(x) \quad (x \in \Omega_a), \quad (46)$$

where O_a is an offset that depends on the subdomain number: $O_a = 0$ if $a = 0$ and

$$O_a = I_L(x_{0,L}) + \sum_{d=0}^{a-1} I_{L,d}(x_{d,R}), \quad (47)$$

otherwise. With this separation, the piece $I_{L,a}$ can be computed independently in parallel in each subdomain. After this is performed, the boundary values needs to be communicated to compute the offset of each subdomain O_a and apply it to all the points of each subdomain, again, in parallel.

When solving PDEs it is necessary to specify how to communicate the different subdomains, and this depends on the character of the PDE system. Here, we are going to discuss how to use the multidomain PSC method to solve hyperbolic PDEs. In this case, at the boundaries between the subdomains we have two points, the right boundary of the subdomain to the left and the left boundary of the subdomain to the right, which are identified in these that they represent the same physical point. In principle we have solve the PDEs at both points, but the PDEs themselves

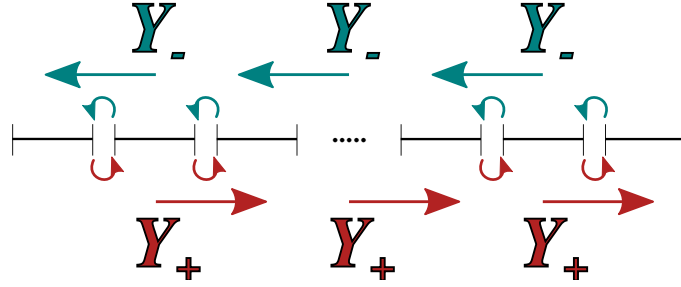


Figure 4: **Diagram of the Multidomain Structure for PSC Methods.** The evolution variables need to be communicated between subdomains using the characteristic variables, Y_- and Y_+ , which have a well defined direction of propagation. The communication is done by copying the boundary values in the direction indicated by the arrows.

impose some constraints on how to assign values of the PDE variables to these two points. To understand how to do this in practice, let us consider a general hyperbolic PDE system in $1 + 1$ dimensions (time t and spatial coordinate x) in first-order form:

$$\partial_t \mathbf{W} + \mathcal{A}[x, \mathbf{W}] \cdot \partial_x \mathbf{W} = \mathcal{S}[x, \mathbf{W}], \quad (48)$$

where \mathbf{W} is the vector of variables, \mathcal{A} is a matrix that determines the characteristic structure (see, e.g. [17] for details) of the PDEs, and \mathcal{S} is a source vector that depends on the coordinate x and the variables \mathbf{W} . The hyperbolicity character of the PDE problem is determined by the following eigenvalue problem:

$$\mathcal{A} \cdot \mathbf{E} = \lambda \mathbf{E}, \quad (49)$$

where \mathbf{E} is a vector in the space of our variables \mathbf{W} . If there is a complete set of eigenvectors and all the eigenvalues are real the system is said to be *strongly hyperbolic*. The eigenvectors of the matrix \mathcal{A} correspond to the different characteristic fields of the system and the eigenvalues to the characteristic speeds associated with the characteristic fields. We can then choose a new set of variables consisting of the characteristic fields, say \mathbf{Y} , which have a well-defined propagation velocity, the eigenvalues λ . Using these these new variables, we can rewrite Eq. (48) as:

$$\partial_t \mathbf{Y} + \mathcal{D}_{\mathcal{A}} \partial_x \mathbf{Y} = \tilde{\mathcal{S}}(x, \mathbf{Y}), \quad (50)$$

where $\mathcal{D}_{\mathcal{A}}$ is the diagonal matrix containing the eigenvalues λ . Given that these eigenvalues represent the propagation velocity of the variables of the problem, some will have positive velocity, let us say \mathbf{Y}_+ , and others will have negative velocity, say \mathbf{Y}_- . This knowledge is crucial to deal with the boundaries in our multidomain framework. The procedure to update the points at the boundaries between subdomains is as follows (see Figure 4): Let us consider two subdomains, Ω_a and Ω_{a+1} , with common boundary points $x_{a,R}$ (right boundary of Ω_a) and $x_{a+1,L}$ (left boundary of Ω_{a+1}). The fields with positive speed, \mathbf{Y}_+ , are evolved at $x_{a,R}$ using the PDEs in Eq. (50) and the values obtained are copied to the corresponding variables at the point $x_{a+1,L}$. Conversely, the fields with negative speeds are evolved at $x_{a+1,L}$ using the PDEs and the resulting values are copied to the corresponding variables at the point $x_{a,R}$. Finally, the characteristic variables are not only important to deal with the boundaries between subdomains, they can also be used to impose boundary conditions at the global boundaries in a clear and simple manner, for instance in/outgoing boundary conditions.

3. The PSC method and Arbitrary Precision

The representation of real numbers, in principle with infinite significant digits, in the limited memory of a computer is a delicate issue. The usual solution is what is called the floating-point representation, similar to scientific notation, where a given real number x can be expressed as:

$$x = \left(1 + \sum_{i=1}^{b_m-1} b_i \times 2^{-i} \right) \times 2^E, \quad (51)$$

where b_m is the total bits of the mantissa and E the exponent stored. The number of bits dedicated to E is important because it establishes the maximum range of our variables. However, we are more interested in the influence of b_m . This value sets our machine precision, also known as round-off error, as:

$$\text{error} = \lceil \text{bits} \cdot \log_{10}(2) \rceil. \quad (52)$$

The standard numerical precisions that we take as a reference are: *single precision*, where the number of mantissa bits is 24 (eight significant digits) and *double precision*, with 53 mantissa bits corresponding to 15/16 significant digits.

In this section, we discuss the advantages of using the PSC method in combination with computations with arbitrary numerical precision for numerically solving (hyperbolic) PDEs. Moreover, we show how some of the PSC techniques described in the previous section perform for different bit precisions. We also compare the results using the PSC method with those from other discretization methods. All the PSC algorithms have been implemented with the **ANETO** library for PSC methods. Details about the structure of the library can be found in Appendix A.

3.1. Numerical Integrals

We start by studying the precision in the computation of an integral using the quadrature methods described previously. As a test function we take a simple cosine function:

$$f(x) = \cos(x), \quad (53)$$

We then consider the question of computing the integral of this function over the spectral domain, i.e. $[-1, 1]$. The results are shown in Figure 5. The plot on the left shows that as long as one includes enough points in the collocation grid, the error scales with the round-off error as expected. This is true even for a number of collocation points as low as $N = 47$ up to 260 bits of precision, when the error saturates because the discretization error becomes more important than the round-off error. We have also seen that it is enough to use $N = 71$ collocation points to decrease the error up to 10^{-120} . The same behaviour is shown on the right plot of Figure 5 when using the multidomain scheme with only four subdomains and $N = 23$ and $N = 47$ collocation points per subdomain. In the first case, $N = 23$, the discretisation error is reached around 10^{-50} but, for the second one, $N = 47$, we can easily reach again 10^{-120} . The horizontal lines in the figure show the round-off error for the single, double, and quadruple precisions respectively, which is obviously much higher than the error we can reach using arbitrary precision.

Notice that thanks to the exponential convergence of PSC methods it is easy to obtain very small errors with a relatively low number of collocation points. In the previous example we have reached a very small numerical error with less than two hundred collocation points. Although the integral under consideration involved a simple function, we have checked that the same is true independently of the integrand, just restricting ourselves to functions that have no pathological differential behaviour. Figure 5 seems to indicate that in the multidomain scheme the total number of collocation points needs to be higher to obtain a similar error level as in the single domain case, but it has the advantage that, in general, it is faster and more flexible for other operations.

The accuracy that PSC methods are capable to reach is even more clear when we compare it with other discretization methods. In the left plot of Figure 6, we compare the results obtained using the **ANETO** library to Newton-Cotes (NC) formulae [18] of fourth and eleventh orders. In both cases, we set manually the points near the boundaries of the subdomain to avoid the problems associated with the borders. The NC formula of eleventh order seems to be good enough to achieve a reasonable accuracy but the polynomial dependence of the error makes it very difficult to reach accuracies beyond 10^{-50} , while with the PSC method accuracies of the order of 10^{-300} are within reach by using just 100 collocation points. This is not a completely fair comparison because the NC formulae can be easily implemented and evaluated while the corresponding computations within the framework of the PSC method are much more difficult to implement (see the discussion in Sec. 2). Taking this into account, in the right plot of Figure 6 we have compared both methods with respect to the computational time that they require. In the case of the PSC method, we distinguish two cases depending on whether we use the FFT transformation or a matrix transformation between the physical and spectral representations. Although this the comparison more balanced, the conclusion turns out to be the same, even when we use the matrix transformation in the PSC method, which makes the computations slower than when we use the FFT transformation.

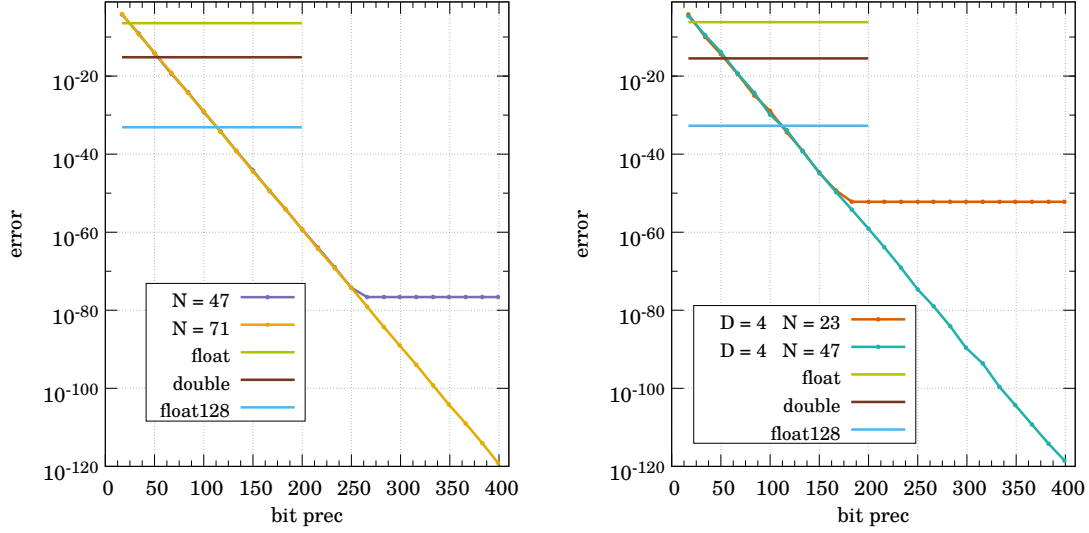


Figure 5: **Maximum Error in the computation of an Integral for Different Bit Precision.** The left plot shows the error made by the integration routine for a cosine function integrated on a single Lobatto-Chebyshev collocation grid. The plot on the right shows the same error but when using the multidomain PSC method. In both cases, the points show the errors made for two different number of collocation points with respect to the bit precision used. The horizontal lines in the plots show the error for single, double, and quadruple precision.

3.2. Solving Ordinary Differential Equations with the PSC method

In order to illustrate the use of the PSC method for the resolution of ODEs we consider an example of a second-order linear ODE that has an analytical solution that we can use to compare with numerical results. The ODE is given by:

$$\frac{d^2 f(x)}{dx^2} + \frac{df(x)}{dx} = e^x, \quad x \in [-1, 1], \quad (54)$$

with boundary conditions,

$$f(-1) = \frac{e}{2}, \quad \frac{df}{dx}(-1) = \frac{e}{2}, \quad (55)$$

and the solution is simply:

$$f(x) = \frac{1}{2} e^x. \quad (56)$$

The ODE in Eq. (54) can be discretised using the PSC method by asking it to be satisfied at the collocation points $\{X_i = x_i\}$ of a Lobatto-Chebyshev grid:

$$\sum_{j=0}^N (\mathcal{D}_{xx}^{ij} + \mathcal{D}_x^{ij}) f^j = e^{x_i}, \quad (57)$$

where \mathcal{D}_x^{ij} and \mathcal{D}_{xx}^{ij} are the first- and second-order differentiation matrices respectively, and f^i are the collocation values of the “unknown” function $f(x)$. The differentiation matrices are given by Eqs. (35) and (36). We compare the results of the PSC method to those from a sixth-order Finite Differences (FD) scheme with uniformly distributed grid points. For this FD scheme, the first-order differentiation matrix for the interior points can be written as:

$$\sum_{j=0}^N \mathcal{D}^{ij} f^j = \frac{-f^{j-3} + 9 f^{j-2} - 54 f^{j-1} + 54 f^{j+1} - 9 f^{j+2} + f^{j+3}}{60 \Delta x}. \quad (58)$$

The comparison between the two methods can be seen in Figure 7 where we show the error as a function of the number of grid points used in each method. As we already saw in the previous section, the exponential convergence of the

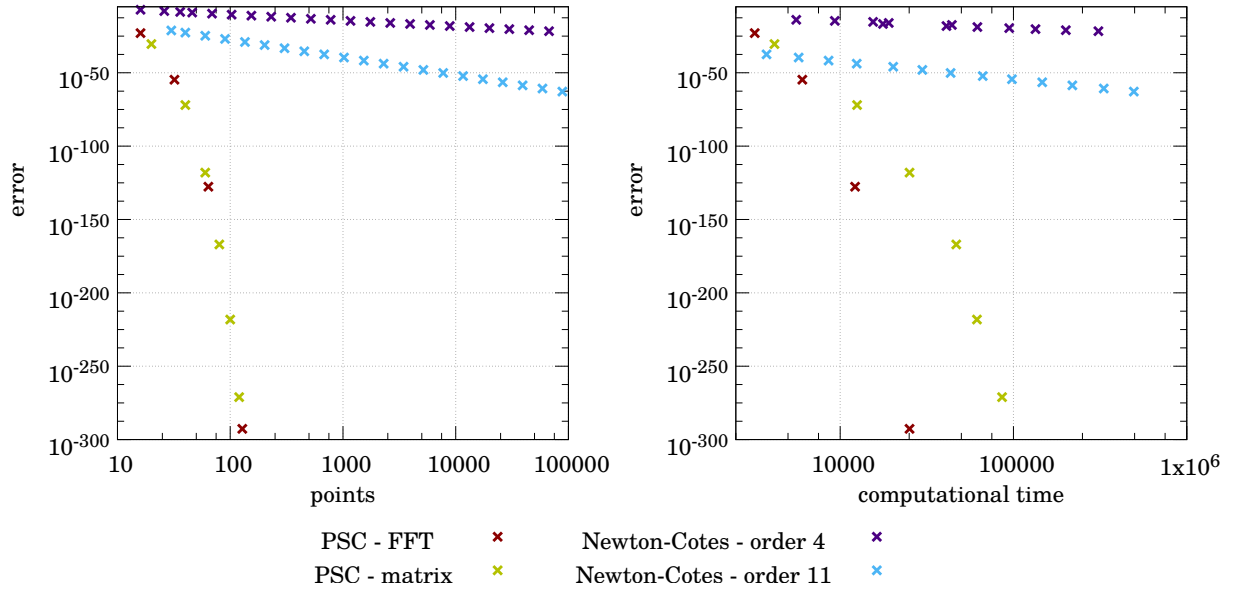


Figure 6: **Comparison between the PSC method and Newton-Cotes formulae for numerical integrals.** In the plots we compare the error made in the computation of our test integral using the PSC method, both using the matrix transformation (yellow points) and the FFT transformation (red), and two different Newton-Cotes formulae, one of fourth order (dark blue) and another one of eleventh order (light blue). In the left plot we compare the same error taking in account the computational time used by the different methods.

PSC method gives us a very good accuracy with a relatively very small number of collocation points. This is crucial in this case because the solution involves inverting a matrix and therefore, its size is crucial. Actually, it is important to realize that the matrix in the case of the PSC method is sparse while in the FD method its sparsity will depend on the stencil (number of points needed for each derivative evaluation) but in general the cost of inverting the matrix will be bigger in the PSC method. But this advantage turns out not be important when we consider high accuracies where the spectral convergence of the PSC method outperforms the FD method.

3.3. Double versus Arbitrary Precision: Computational Time

We have just seen that arbitrary precision arithmetics in combination with the PSC method is a powerful computational tool. The next step is to study the computation cost of using it. Most of the available computers nowadays use a 64-bit processor that is highly optimised to work with double precision. Going beyond this precision usually requires a software implementation that slows down the computation. The question is how much slow down can be expect depending on the precision that we need to use.

We use the simple test case of the integral of Eq. (53) to quantify the cost for three different grid configurations. The results are summarized in Figure 8, where we can see how much slower is the use of arbitrary precision as compared with the standard double precision. In the range analysed, until 512 bits or around 150 significant digits, the computational time seems to increase linearly, being a factor 150-300 times slower than the double precision case. Moreover, we have to take into account that in order to take advantage of the additional significant digits we need to increase the number of subdomains and/or collocation points. These are considerations that one needs to take into account to estimate whether arbitrary precision can be a good solution for a given numerical problem.

Looking at Figure 8, it is also worth mentioning the small jumps in the computational time. Although the general behaviour is linear, at small scales the function is more or less flat, increasing in multiples of 64 bits. This is not surprising because the tests have been done using a 64-bit processor and are related to the way the library uses double precision numbers to stored the arbitrary floating points variables.

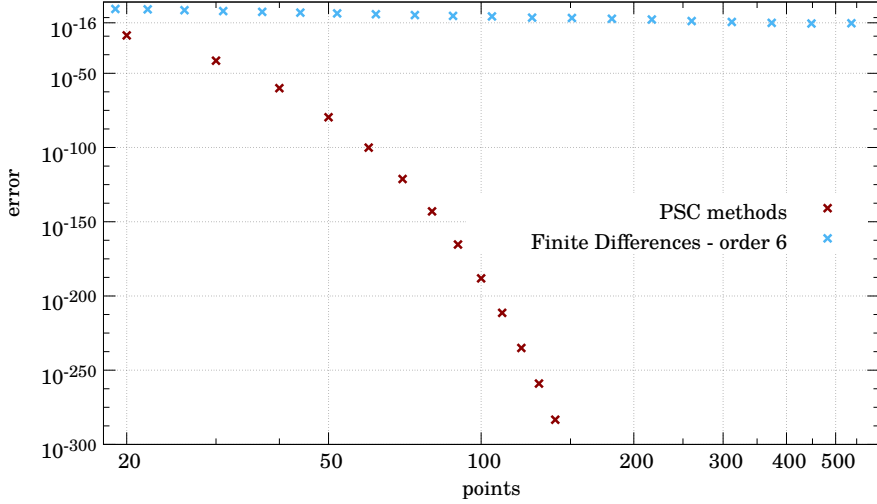


Figure 7: **Comparison of the performance of the PSC and FD methods for ODE solving.** The plot shows error in solving the second-order ODE in Eq. (54), with boundary conditions in Eq. (55) and analytic solution in Eq. (56). This error is understood here as the difference between the numerical and analytic solutions for both the PSC and FD methods. The plot shows how this error changes with the number of grid points used.

3.4. Shared-memory parallelization of PSC computations using arbitrary precision

In the previous subsection we have seen that a problem with the use of arbitrary precision is the computational speed. Given that current computer processors are designed for 64-bit precision computations, most of the arbitrary precision libraries emulate this using symbolic calculations or a software layer that implements the arbitrary precision operations. Both options significantly slow the computations, in our case around 150 – 300 times. In order to alleviate this drawback we can resort to parallelization. Indeed, the use of parallel computing adapts perfectly to our pseudo-spectral multidomain scheme because most our computations are done independently within each of the subdomains. In this sense, we think that shared-memory parallelization, and more specifically, the broadly used application programming interface OpenMP [19] is the simplest option to profit from the independence of the subdomains adding the minimum possible communication overhead. We have carried out a number of numerical experiments using OpenMP. The measure of computational time speedup as we increase the number of cores, p , that we use, S_p , is defined as:

$$S_p = \frac{T}{T_p}, \quad (59)$$

where T is the time used by a sequential computation and T_p is the time corresponding to a computation that uses p cores. Of course, the ideal unreachable limit is $S_p = p$.

We have performed tests using OpenMP for the integration and differentiation operations described above in this article, both with double precision and quadruple precision (`float128`). The results are shown in Figure 9 where the computational speedup, S_p , as a function of the number of cores p . The ideal scaling is shown as a dash line in the plot and we can see that we are very close to the maximum speed-up. It is also interesting to notice that the differentiation computations are closer to full parallelism than the integration ones. This is expected from the fact that this operation can be fully carried out independently at each of the subdomains while for integration we need to communicate the partial integrals.

Up to here we have discussed how to parallelize the operations using the multidomain framework so that each core is in charge of the operations of one or more subdomains, but in any case, the subdomain is the minimum unit of parallelization. This approach does not address the principal cause in the slow down, the emulation of the fundamental operations. This is a question currently under investigation in projects like [20], where they described the arbitrary

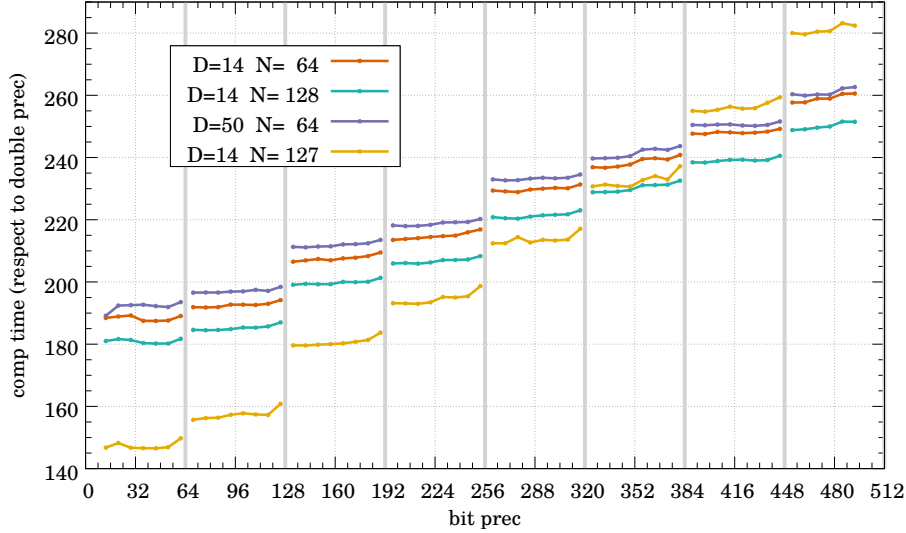


Figure 8: **Computational Time of Arbitrary Precision.** The plot shows the computational time for the integration test discussed in Sec. 3.1 for four different grid configurations with D subdomains and N collocation points. All the times are normalised with respect to the computation time that double precision takes (they are not absolute computational times). Looking at the global behaviour, the computational time appears to be linear with the bit precision. The vertical lines just separate multiples of 64 bits. The computational time increases in these boundaries as expected due to CPU architecture. The runs with $N = 64$ and $N = 128$ collocation points per subdomain use the FFT transformation between the physical and spectral representations, while the one with $N = 127$ collocation points per subdomain uses the matrix transformation between representations. As a consequence, the simulations with $(D, N) = (14, 127)$ are much slower, in absolute computational time, than the ones with $(D, N) = (14, 128)$.

precision numbers as an expansion of double precision numbers of different magnitudes and then take advantage of graphics processing units (GPUs) parallel computing to implement this basic operations.

3.5. Multidomain Derivatives: The Dual Grid

The computation of derivatives at points near the subdomain boundaries tends to accumulate a significant error, in some cases it can be one or two orders of magnitude higher than in other central regions of the subdomain. This phenomenon, known as Runge’s phenomenon [21, 22], gets worse as we increase the number of collocation points. As we already mentioned in Secs. 2.1 and Appendix A.2, we can deal with this problem by using a dual-grid structure as the one shown in Figure 3. We have carried out several numerical experiments to assess the use of the dual-grid structure by comparing with computations in a single grid. The results are summarized in Figure 10. In the top-left plot we show the error in the computation of a derivative on a physical domain that has been divided into ten subdomains. It is easy to find in the plot the location of the boundaries between the subdomains since the error exhibits a peak of more than one order of magnitude in most of the cases. The brown line of the bottom-left plot shows the error when we perform the same computation but using the dual-grid scheme. As we can see, the peaks has completely disappeared and the error in the derivative looks now quite flat. This improvement can be seen on the top-right plot of Figure 10, where we present the ratio between the differentiation errors with and without using the dual grid. Near the boundaries our computation has improved between one and two orders of magnitude in terms of the error. We have done the same comparisons for the second derivative, which is shown in the bottom-right plot. As we can see, the improvement is even better than in the case of the first-order derivative, and the error at all the boundaries has been reduced in two/three orders of magnitude.

4. Applications to Numerical Relativity: Gravitational Collapse

The main motivation of this work and the reason why we have developed the numerical tools described here is the study of gravitational collapse in the framework of the General Theory of Gravitation, known simply as General

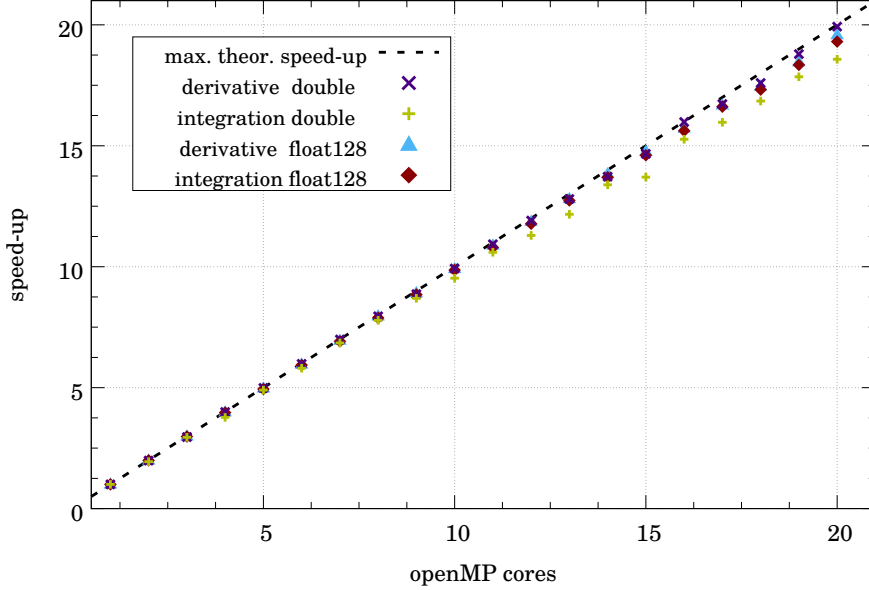


Figure 9: **Speed-up with OpenMP for PSC multidomain computations.** The plot represent the speed-up defined in Eq. (59) at integral and derivative routines for double and quadruple precision. Derivatives present a better speed-up but both cases show that multidomain is a very good option for parallelization.

Relativity (see e.g. [23, 24, 25, 26] for general introductions). The main idea behind General Relativity is that gravity is not a force but a manifestation of the curvature of the spacetime as a unique object. Then, the mathematical description uses the language of differential geometry where the spacetime is Lorentzian manifold of 3 + 1 dimensions and gravitation is described a the Lorentzian² metric tensor associated with it, $g_{\mu\nu}$ ($\mu, \nu = 0, 1, 2, 3$). It turns out that complex problems (for instance, problems with low degree of symmetry) in General Relativity require numerical methods to be solved, and given the special mathematical description of the theory a new area of research was created, Numerical Relativity (see, e.g. [27, 28, 29]), whose main aim is solving the PDEs for the metric tensor: Einstein field equations. These are tensorial equations that connect the energy-momentum distribution in the spacetime with the curvature of the spacetime as a differential manifold. They tell spacetime how it has to be curved due the presence of energy and momentum and, at the same time, they matter how to “move” in the curved geometry of spacetime. These continuous feedback between geometry and matter dynamics makes the equations nonlinear. They can be expressed as follows:

$$R_{\mu\nu} - \frac{1}{2}g_{\mu\nu}R = 2T_{\mu\nu}, \quad (60)$$

where $R_{\mu\nu}$ is the Ricci Tensor associated with the metric tensor $g_{\mu\nu}$ (both are symmetric tensors); R is the scalar of curvature, which can be obtained as the trace of the Ricci tensor using the inverse metric tensor: $R = g^{\mu\nu}R_{\mu\nu}$. Both the Ricci tensor and the scalar curvature are obtained exclusively from the metric tensor and its derivatives up to second order. Finally, $T_{\mu\nu}$ is the energy-momentum tensor, another symmetric tensor, that tells us the distribution of mass, energy, and momentum in the spacetime. Despite the complexity of this equations, they constitute a couple system of second-order non-linear PDEs, a number of exact solution have been found (see [30] for a very broad account), some of them of great significance like the ones that describe black holes and different large-scale cosmological scenarios. But, as we have already mentioned, most of these exact solutions were found by simplifying in one way or another the Einstein field equations.

Numerical Relativity is nowadays a mature field where a number of techniques have been developed for solving different kinds of problems, from cosmology to the emission of gravitational radiation. The focus of this paper in on

²The signature of the metric is $(-1, 1, 1, 1)$ and hence the metric it is not a positive definite matrix.

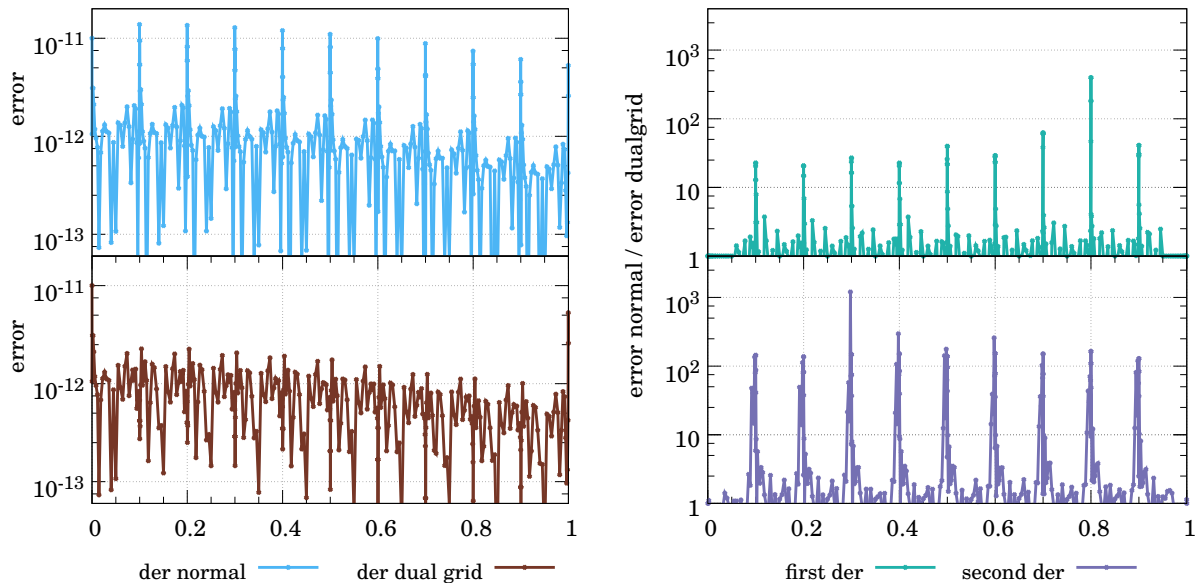


Figure 10: **Dual-Grid Differentiation.** The plots on the left show the error in the first derivative computed with the dual-grid setup (bottom) or without it (top). It can be seen that in the boundaries across subdomains there is a huge reduction of the error. The magnitude of the improvement can be seen in the top right plot. The quotient of the error in both cases quantifies the improvement in the points near the boundaries between one and two orders of magnitude. The bottom right plot shows the same for the second derivative where the improvement increases from two to three orders of magnitude.

the subject that inaugurated the field of Numerical Relativity with one of the main results found so far: The finding of critical behaviour in gravitational collapse [31]. We are going to apply the numerical techniques described above to gravitational collapse in the context of Anti-de Sitter (AdS) spacetimes, which have attracted a lot of attention recently due to its applications to string theory and the gauge-gravity duality. Given the high demands of precision of the problem of gravitational collapse in AdS spacetimes we decided to use PSC methods and later, arbitrary precision computations. This is not the first time that PSC methods have been used in Numerical Relativity, they have previously used successfully for the simulation of the collision of orbiting binary black holes [32, 33] (see also e.g. [2, 34, 35, 36, 37]). We have applied these methods to the study of the gravitational collapse of scalar fields in AdS spacetimes. The main physical results were published in [7, 8]. In this section we describe how the PSC method in combination with arbitrary precision can be crucial in order to obtain results that otherwise would not be possible or very costly from the computational point of view. We are going to show two different mathematical formulation of the problem of gravitational collapse in AdS spacetime, and also of the evolution of perturbations in AdS spacetime, that lead to two completely different numerical implementations.

4.1. Gravitational Collapse

We are going to start with the classical problem of gravitational collapse in a flat (Minkowski) spacetime. The collapsing energy-momentum distribution is the one of a massless real scalar field. Considering initial states such that the initial data is smooth, there are only two possible states of the evolution: (i) Collapse of the scalar field configuration and the formation of a Black Hole (BH). (ii) Dispersion of the scalar field towards infinity and the asymptotic end state will be flat spacetime. Whether we end up in one case or the other depends on the energy density of the initial configuration. An interesting question is what separates these two very different outcomes of the evolution. M. Choptuik [31] carried out a systematic numerical study of this question and found that the dependence of the final state on the initial data is through a single (arbitrary) parameter. He found that in the threshold between collapse and dispersion there is a one-parameter family of critical solutions that exhibit a naked singularity. He also found that the mass of the collapsed configurations near the threshold exhibit an scaling with a universal

exponent. These unexpected results attracted a lot of attention to this problem and helped a lot in the development of Numerical Relativity. A detailed review of critical gravitational collapse for different types of matter fields and spacetime configurations in General Relativity can be found in [38, 39]. In what follows we will restrict ourselves to problems in spherical symmetry, like in the initial studies by Choptuik, and hence the resulting PDEs will be in $1 + 1$ dimensions (time and radial coordinate). Apart from this we will not make any further simplification of the problem.

The first step towards numerical simulations of gravitational collapse is to choose an adequate formulation of the Einstein field equations. We choose what is called a characteristic approach to the problem (introduced in [40, 41, 42]). The main idea of this approach is to set initial data on a null slide instead of a constant time slide. The difference is that the normal to a null slide is a light-like one-form while the normal to constant time slide is a space-like one-form, like in a standard initial Cauchy problem. The main advantage of the characteristic formulation is its ability to approach the BH formation much more efficiently than a typical Cauchy one. In this sense it is worth mentioning that the initial Choptuik study [31] was based on a Cauchy formulation and used adaptive mesh refinement. Later, Garfinkle reviewed the problem by using a characteristic approach [42] and recovered some of the main results without the need of refinement, which show the power of the characteristic formulation for this type of problems. We also confirmed the performance of the characteristic approach by evolving scalar fields, not in asymptotically-flat spacetimes but in Asymptotically-AdS (AAdS) spacetimes [7, 8]. However, the setup we developed in [7, 8] is not suitable for the use of PSC methods so we developed a FD numerical code. In this section we present an improved characteristic scheme that is adapted for the use of PSC methods.

The formulation of the characteristic problem goes as follows. We consider a self-gravitating massless scalar field, ϕ . The PDEs that we need to solve are the coupled system formed by the Einstein field equations in Eq. (60) and the equations for the scalar field which come from the energy-momentum conservation equations. These equations derive also from the Einstein field equations and they are a consequence of the fact we mentioned above that the spacetime tells matter how to move. These equations come from the covariant divergence of the Einstein field equations in Eq. (60):

$$T_{\mu\nu}{}^{;\nu} = 0, \quad (61)$$

where we assume the Einstein convention that there is summation over repeated indices³. Moreover, the semicolon in this equation denotes covariant differentiation which, together with the summation convention, this equation is telling us that the covariant divergence of the energy-momentum tensor must vanish. The energy-momentum tensor for a scalar field is given by

$$T_{\mu\nu} = \phi_{;\mu}\phi_{;\nu} - 2 g_{\mu\nu}\phi_{;\alpha}\phi^{;\alpha}, \quad (62)$$

where the covariant derivatives on the scalar field are equivalent to partial derivatives: $\phi_{;\alpha} = \partial\phi/\partial x^\alpha \equiv \phi_{,\alpha}$. Then, the resulting field equation for the scalar field is:

$$\square\phi \equiv \phi_{;\mu}{}^{\mu} = 0. \quad (63)$$

Now, in order to introduce the characteristic formulation we need to introduce an adequate coordinate system. We consider double-null coordinates for the time-radial section together with spherical coordinates for the spheres of symmetry of the problem. Then, the line element of the spacetime, which is equivalent to specify the metric tensor, in those coordinates is:

$$ds^2 = g_{\mu\nu}dx^\mu dx^\nu = -2f(u, v) r_v(u, v) dudv + r^2(u, v)d\Omega^2, \quad (64)$$

where (u, v) are the double-null coordinates and $d\Omega^2 = d\theta^2 + \sin^2\theta d\varphi^2$ is the line element of the unit 2-sphere. Moreover, f and r are two arbitrary functions of (u, v) and r_v denotes the partial derivative of r with respect to the null coordinate v . The idea of a double-null foliation is to use both directions of the propagation of light rays, ingoing and outgoing, as part of our system of coordinates. In Figure 11 we show a representation of this idea for the case of an empty spacetime. In our case, the spacetime is curved by the presence of the massless scalar field ϕ and hence (u, v) would not be perpendicular to the (r, t) coordinate lines.

To obtain the set of PDEs for the components of the metric tensor (essentially the functions f and r) and the scalar field we have to introduce Eq. (64) into Eqs. (60) and (63). In order to reduce the order of the equations and to

³For instance, for a tensor $A_{\mu\nu}$ we use the notation: $\sum_{\mu=0}^3 A^\mu{}_\mu \equiv A^\mu{}_\mu$.

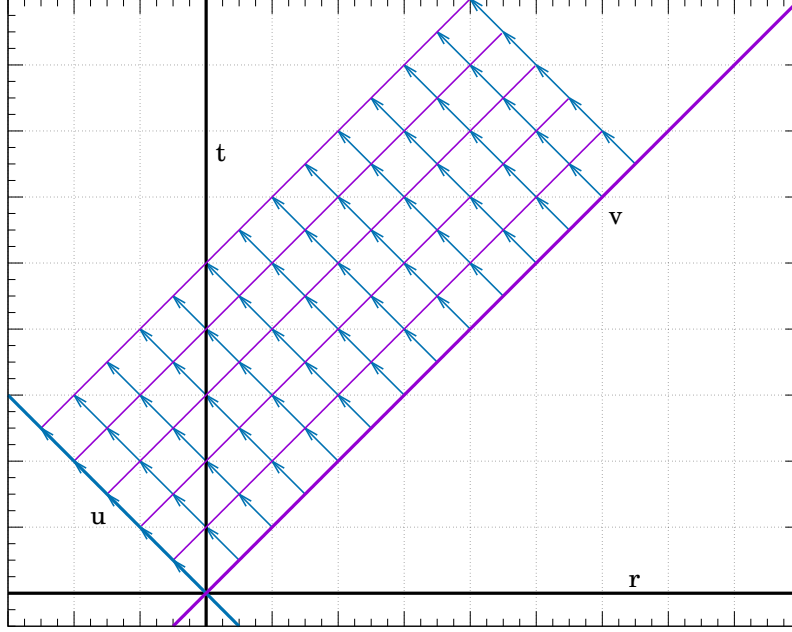


Figure 11: **Scheme of an Evolution using Double-Null Coordinates.** The horizontal and vertical lines are the axis corresponding to the time and radial coordinates, (r, t) . In a characteristic problem, we set our initial conditions on a $u = \text{const}$ slide (purple thick line) and evolve each point in the direction indicated by the arrows. This scheme is strictly valid in the case of an empty spacetime where constant null coordinate lines form 45 degrees with respect to the axes (r, t) . In a general case, the (u, v) coordinates will be not be straight but the idea is essentially the same.

decouple them we introduce the following new variables associated with the scalar field ϕ (from now on the u and v subscripts denote partial differentiation with respect to these coordinates):

$$h = \frac{(r\phi)_v}{r_v}, \quad (65)$$

$$\bar{h} = \phi, \quad (66)$$

and also a new metric variable:

$$\bar{f} = -2r_u. \quad (67)$$

With these new variables, the vv and the uv components of the Einstein field equations can be written as:

$$f_v = \frac{f r_v}{r} (h - \bar{h})^2, \quad (68)$$

$$\bar{f}_v = \frac{r_v}{r} (f - \bar{f}). \quad (69)$$

In the characteristic formulation we are using we prescribe initial conditions for the variable h on an initial $u = u_i = \text{const}$ null slide, that is $h(u_i, v)$. We also need to prescribe $r(u_i, v)$ and $r_v(u_i, v)$ on that initial null slide. With all this information we can obtain the rest of variables, at the same null slide $u = u_i$, using the equations above. The

expressions for h , f , and \bar{f} are:

$$\bar{h}(u_i, v) = \frac{1}{r} \int_{v_o(u_i)}^v d\tilde{v} h(u_i, \tilde{v}) r_v(u_i, \tilde{v}), \quad (70)$$

$$f(u_i, v) = f(u_i, v_o(u_i)) \exp \left\{ \int_{v_o(u_i)}^v d\tilde{v} \frac{r_v}{r} (h - \bar{h})^2 \right\}, \quad (71)$$

$$\bar{f}(u_i, v) = \frac{1}{r} \int_{v_o(u_i)}^v d\tilde{v} f(u_i, \tilde{v}) r_v, \quad (72)$$

where $v_o(u_i)$ and $f(u_i, v_o(u_i))$ are the values of v and $f(u, v)$ respectively, at the origin $r = 0$ on the null slide $u = u_i$. By looking at these expressions we realize that we need to guarantee the regularity of the different quantities at the origin, which translates into imposing the conditions $\bar{h}(u_i, v_o(u_i)) = h(u_i, v_o(u_i))$ and $\bar{f}(u_i, v_o(u_i)) = f(u_i, v_o(u_i))$. In this way, all the equations have a finite limit when we approach the origin $r = 0$. However, for numerical purposes it is not convenient to have divisions where both numerator and denominator tend to zero. This may be particularly problematic with Eq. (72), but it can be transformed by using integration by parts and taking the right limits. The result is:

$$\bar{f}(u_i, v) = f(u_i, v) - \frac{1}{r} \int_{v_o(u_i)}^v d\tilde{v} f(u_i, \tilde{v}) r_v [h(u_i, v) - \bar{h}(u_i, v)]^2. \quad (73)$$

Once we have (h, \bar{h}, f, \bar{f}) at the null slide $u = u_i$ we can evolve them to the next null slide by using the evolution equation for the scalar field, i.e. Eq. (63), which comes from the energy-momentum conservation equation (61). At this point it is important to comment that, due to the spherical symmetry we have imposed on the spacetime and matter fields, only the scalar field has true dynamics. By this we mean that the true degrees of freedom of the gravitational field, as described by the metric tensor $g_{\mu\nu}$, are not excited in the case of spherical symmetry. In other words, there are no gravitational waves present, only scalar field waves. Said that, the evolution equation to pass from a null slide to the next one in our characteristic formulation is given by:

$$h_u = \frac{1}{2r} (f - \bar{f})(h - \bar{h}). \quad (74)$$

In addition, from Eqs. (67) and (69) we can obtain the evolution equations for r and r_v :

$$r_u = -\frac{1}{2} \bar{f}, \quad (75)$$

$$(r_v)_u = -\frac{1}{2} r_v \left[\frac{f - \bar{f}}{r} \right]. \quad (76)$$

The only piece missing in this characteristic evolution scheme is the value of $f(u_i, v_o(u_i))$ that appears in Eq. (71), which corresponds to the value of f at the origin on the null slide $u = u_i$. This is a freely specifiable quantity that reflects the residual *gauge* freedom that we have in the choice of the null coordinate v . This, in turn, can be seen as the remaining gauge freedom in completely specifying the radial function r in our characteristic formulation. In particular, it allows us to specify the location of the origin $r = 0$ at the null slides $u = \text{const}$. Or in other words, the freedom in choosing the motion of the origin ($r = 0$) as we evolve from one null slide to the next one. Indeed, since $r = r(u, v)$, and assuming that $v = v_o(u)$ corresponds to the location of the origin, i.e. $r(u, v_o(u)) = 0$, the equation of motion of the origin as we move through the spacetime foliation in null slides $u = \text{const}$. is given by:

$$\frac{dv_o(u)}{du} = - \left. \frac{r_u}{r_v} \right|_{v=v_o(u)} = \left. \frac{f_o}{2r_v} \right|_{v=v_o(u)}, \quad (77)$$

where we have used Eq. (75). We can then use this freedom to make the origin move, for instance, with a uniform speed. To achieve this we just need to choose the freely specifiable quantity $f(u, v_o(u))$ as:

$$f(u, v_o(u)) = 2 \left. r_v \right|_{v=v_o(u)} \implies v_o(u) = v_o(u_i) + u. \quad (78)$$

On the other hand, in the simulations we have carried out we have used a Gaussian packet as initial data for the scalar field:

$$h(u_i, v) = \epsilon e^{-\frac{(v-b)^2}{\omega^2}}, \quad (79)$$

where the amplitude ϵ , the width ω , and the shift b are freely specifiable parameters of this family of initial data. We have performed an evolution taking: $\epsilon = 2.00$, $b = 0.15$ and $\omega = 0.05$. This is an initial configuration above the critical threshold and hence it will collapse and form an apparent horizon (AH). The evolution is carried out using a standard Runge-Kutta 4 (RK4) algorithm. In our formulation the formation of an AH happens when the following condition is fulfilled:

$$r_v \longrightarrow 0, \quad \text{or equivalently,} \quad \frac{\bar{f}}{f} \longrightarrow 0. \quad (80)$$

This limit cannot be reached with our system of coordinates although we can approach it as much as we want. Then, we assume that an AH has formed when the quantities in the AH condition above reach a value less than 10^{-8} . At that point we stop the simulation.

The characteristic formulation of the problem is now complete and it is well-adapted for its implementation using the PSC method for the discretization in the v coordinate (we evolve from one null slice $u = \text{const.}$ to the next one by using a traditional ODE solver as the RK4). We have implemented this formulation using the PSC method and arbitrary precision tools described in previous sections. Using the spectral representation, Eq. (8), the error can be estimated from the absolute value of the last spectral coefficient. The value of the coefficients a_n ($n = 0, \dots, N$) decay exponentially, reaching or not the round-off error. If round-off is not reached, the last spectral coefficient represents an estimation of the truncation error incurred in ignoring the rest of terms in the spectral series. Otherwise, if the last coefficient is the round-off error the last coefficient represents the precision reached. In both cases, it can be used for a good estimation of the error. We have performed evolutions using the initial data specified in Eq. (79). In Figure 12 we show the error in the location of the AH at the end of the evolution in terms of the number of collocation points per subdomain. Since we have different errors at each subdomain, we take the highest of all of them, which corresponds to the subdomain where the collapse takes place. In Figure 12 we only show the error associated with the function r_v , to monitor the first condition in Eq. (80), because it is the one that has the highest error of all the three evolution variables.

Moreover, on the left plot of Figure 12, we use a setup with $D = 20$ subdomains and we change the number of collocation points for different bit precision. In this plot we have used a log scale in the vertical axis. In all the cases, the error has an exponential decay (spectral convergence) until we reach the precision limit which, of course, improves as we increase the number of bits of our data types. The first one represents a 53 bit precision, equivalent to the double standard, which allows us to obtain a maximum precision of 10^{-10} - 10^{-11} . Notice that this is few orders of magnitude above the theoretical limit of sixteen digits. This fact is not surprising since we have to consider that during the evolution the numerical noise piles up, reducing the maximum precision. In addition, the number of subdomains used in our test evolutions is not optimal. This is just a comparison of the same exact set up for several bit precisions. Increasing the number of significant bits we improve the maximum error and with 150 bits (around 45 significant digits) we easily decrease the error up to almost 10^{-40} . On the right plot of Figure 12 we study the influence of the number of subdomains in the error as we change the number of collocation points per subdomain but keeping the number of subdomains constant. The error presents an exponential decay $\Delta r_v \approx \exp(-\alpha N)$. Varying the number of subdomains changes the factor of the exponential decay, α . In this case we can reach the minimum error adding subdomains with less collocation points. This can be a good idea considering that adding subdomains has, in general, a linear impact on the computational time while increasing the number of collocation points, N , has an impact of $\sim N \log N$ or $\sim N^2$ depending on whether the operations in the spectral domain are performed using a FFT transformation or a matrix transformation respectively.

4.2. (In)Stability in Anti-de Sitter Spacetimes

In this section we change the physical context of our computations. In the previous section we used simulations of gravitational collapse, and the eventual formation of an AH, in flat spacetime using a characteristic formulation. Now, we present results of the evolution of (exact non-linear) "perturbations" in Anti-de Sitter spacetimes using a Cauchy formulation. Cauchy-type evolutions in spherical symmetry were already done in the study of critical gravitational collapse by Choptuik [31]. In the context of Anti-de Sitter spacetimes they were used to study also the problem of

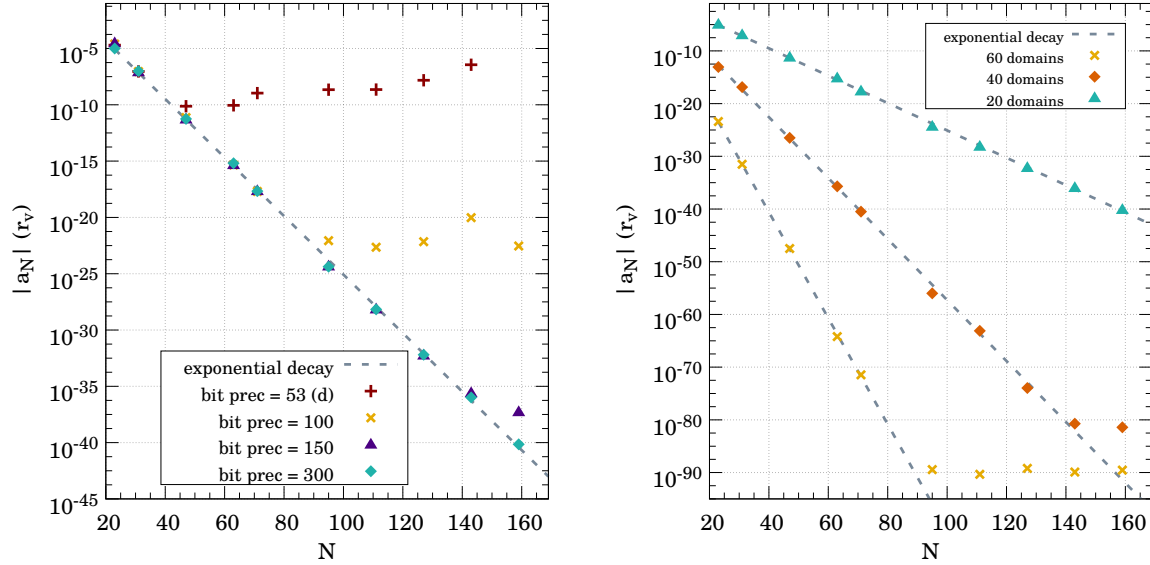


Figure 12: **Convergence in the location of the formation of an Apparent Horizon (AH):** The left plot shows the truncation error (estimated from the last spectral coefficient) at the moment of AH formation for several different grid configurations, all of them with $D = 20$ subdomains. Each data set corresponds to simulations done with different bit precision. The error decays exponentially (spectral convergence) until the maximum precision is reached. On the right plot we show the impact of adding more subdomains. All sets of data exhibit spectral convergence but the number of subdomains has an impact in the α factor of the exponential decay $e^{-\alpha N}$. These simulations are done with 300 bit precision.

critical gravitational collapse in [43]. We adapted this formulation for the use of the PSC method in Refs. [7, 8] and we found new physical features associated with the non-linear evolution. We now present results from a new adaptation of our numerical scheme to include arbitrary precision together with the PSC method.

Anti-de Sitter spacetimes have attracted a lot of attention in the last years, both for the interest in studying the non-linear (in)stability of AdS and for its relevance in the so-called AdS/CFT correspondence (also known as the gauge/gravity duality). The geometry of AdS presents a very interesting property that makes it completely different from other spacetimes: There is a boundary that light-like signals (light rays, massless fields, etc.) can reach in a finite time, but such that for time-like signals (massive particles, massive fields, etc.) it will take infinite proper time to reach it. This property changes completely the landscape of gravitational collapse. In the case of a flat spacetime, as we explained in the previous section, the procedure to study gravitational collapse is to consider an initial profile for the field and then, let it evolve to see whether it collapse forming an AH or, instead, it disperses yielding flat spacetime as the end asymptotic state of the evolution. This two-case scenario changes in AdS spacetimes. Given an initial profile, locally in time, we can also expect that the system will tend to evolve towards to any of the two cases described above. If the field collapses it will form a BH that eventually will set into an stationary state (a Schwarzschild-de Sitter BH). However, if the field tends to disperse, this is not the end of the history. Indeed, in that case the field will disperse, but since we are talking about a massless scalar field, at a finite time it will reach the AdS boundary and it will bounce back and will try to collapse again. Then, again locally in time, there are only two possibilities, i.e. to form an AH or to disperse. If the scalar field tends to disperse it will again reach the AdS boundary in a finite time and bounce back. This process will repeat itself as many times as necessary until the scalar field will finally collapse forming an AH. In the trip to the AdS boundary and back the field, due to the non-linear character of relativistic gravitation, there will be an energy transfer from low frequency (long wavelength) modes towards high frequency (short wavelength) modes, similar to what happens in the onset of turbulence. Due to this analogy, this process that at some point will end in the collapse of the scalar field profile, has been named the *turbulent instability* of AdS spacetime. That is, no matter how small would be the amplitude of the initial profile (perturbation) the field will finally collapse and the end state would be an AdS BH spacetime. Nevertheless, this turbulent instability maybe a generic feature of the dynamics in AdS spacetime but there maybe cases in which it will not take place. The reason is

that some stable configurations have been found for some forms of initial configurations, but the exact extend of these “stability islands” in the parameter space of initial configurations is still under debate. In order to study this question we new extremely long and accurate evolutions. In summary, the end state of the evolution of perturbations in AdS spacetimes is an ideal testbed for numerical techniques that provide high-accuracy, beyond the standard one, as the problem is highly demanding. In order to illustrate this, in this section we present a test case in which we evolve an initial massless scalar field configuration in AdS spacetimes during two of these bounces and compare the accuracy obtained using double precision with the one using 300-bit precision.

Again, we need to solve the Einstein field equations, Eq. (60), coupled to the massless scalar field equation, Eq. (63), as in the previous case but this time the spacetime metric is going to be very different, reflecting the AdS asymptotic structure of the spacetime and the fact that we are going to use a Cauchy-type evolution scheme. With this in mind, the form of the spacetime line element that we consider is:

$$ds^2 = g_{\mu\nu} dx^\mu dx^\nu = \frac{\ell^2}{\cos^2 x} \left(-Ae^{-2\delta} dt^2 + \frac{dx^2}{A} + \sin^2 x d\Omega_2^2 \right), \quad (81)$$

where $A = A(t, x)$ and $\delta = \delta(t, x)$ are two arbitrary metric functions, t is the temporal coordinate, and x is a compactified spatial coordinate in such a way that the AdS boundary is located at $x = \pi/2$. The overall factor contains ℓ , the AdS length scale, which is related to the cosmological constant of the spacetime, $\Lambda < 0$, by the expression: $\ell^2 = -3/\Lambda$. The time coordinate t has an infinite range, i.e. $t \in (-\infty, \infty)$, whereas x , being compactified, goes from $x = 0$ (center) to $\pi/2$ (AdS boundary). We can recover AdS spacetime by setting $A = 1$ and $\delta = 0$.

The system of PDEs that be obtain can be reduced to first-order system that turns out to be strongly hyperbolic. Then, in order to use our multidomain scheme, it is advised to use as variables the eigenfields of this hyperbolic system, also known as the characteristic variables (see Refs. [17, 8] for a proper definition and an exact derivation for our case). The form of the characteristic variables that we use for the scalar field are:

$$U = \frac{1}{\cos x} \left(\phi_x - \frac{e^\delta}{A} \phi_t \right), \quad (82)$$

$$V = \frac{1}{\cos x} \left(\phi_x + \frac{e^\delta}{A} \phi_t \right), \quad (83)$$

where again, the (t, x) subscripts denote partial differentiation. Then, using the (t, x) coordinates and the (U, V) variables, the evolution problem is reduced to the following coupled system of PDEs:

$$U_t = -Ae^{-\delta} U_x - \frac{(3 - 2 \cos^2 x)}{\sin x \cos x} U e^{-\delta} (1 - A) - \frac{Ae^{-\delta}}{\sin x \cos x} (U + V) + \frac{\sin x}{\cos x} U Ae^{-\delta}, \quad (84)$$

$$V_t = +Ae^{-\delta} V_x + \frac{(3 - 2 \cos^2 x)}{\sin x \cos x} V e^{-\delta} (1 - A) + \frac{Ae^{-\delta}}{\sin x \cos x} (U + V) - \frac{\sin x}{\cos x} V Ae^{-\delta}. \quad (85)$$

It is also convenient to introduce the following normalized variable associated with the scalar field:

$$\psi = \frac{\phi}{\cos^2 x}. \quad (86)$$

The scalar field satisfy both an evolution equation:

$$\psi_t = \frac{Ae^{-\delta}}{2 \cos x} (V - U), \quad (87)$$

and also a constraint equation (one that does not contain time derivatives, only spatial derivatives):

$$\psi_x = 2 \frac{\sin x}{\cos x} \psi + \frac{1}{2} \frac{U + V}{\cos x}. \quad (88)$$

Then, we can solve for ψ either by evolving Eq. (87) or by solving this constraint equation. Regarding the metric functions, as we mentioned above, we do not expect to have hyperbolic equations for them since in spherical symmetry

we do not have the true gravitational degrees of freedom. Indeed, we can obtain also constraint equations for both δ and A :

$$\delta_x = -\frac{1}{2} \sin x \cos^3 x (V^2 + U^2). \quad (89)$$

$$A_x = \frac{1 + 2 \sin^2 x}{\sin x \cos x} (1 - A) - \frac{A}{2} \sin x \cos^3 x (V^2 + U^2), \quad (90)$$

from which $\delta(t, x)$ and $A(t, x)$ are given by the following integrals:

$$\delta(t, x) = \int_x^{\frac{\pi}{2}} dy \sin y \cos^3 y \left(\frac{U^2 + V^2}{2} \right), \quad (91)$$

$$A(t, x) - 1 = -\frac{\cos^3 x e^\delta}{\sin x} \int_0^x dy e^{-\delta} \sin^2 y \left(\frac{U^2 + V^2}{2} \right), \quad (92)$$

where the boundary conditions are $A = 1$ both at $x = 0$ and $x = \pi/2$ and we have chosen $\delta(\pi/2) = 0$, fixing the time coordinate t as the proper time at the AdS boundary. Then, the Cauchy evolution goes as follows: (i) We prescribe initial data at an initial $t = t_o$ const. Cauchy surface for (U, V) , i.e. $U(t_o, x)$ and $V(t_o, x)$. (ii) Using equations (88), (91), and (92) we find $\psi(t_o, x)$, $\delta(t_o, x)$ and $A(t_o, x)$. (iii) With this we evolve (U, V) from t_o to $t_o + \Delta t$ using the evolution equations (84) and (85) and the boundary conditions. In our numerical simulations we have used the following family of Cauchy initial data:

$$U(t_o, x) = \epsilon \exp\left(-\frac{4 \tan^2 x}{\pi^2 \sigma^2}\right), \quad (93)$$

$$V(t_o, x) = -U(t_o, x), \quad (94)$$

where the freely specifiable parameters ϵ (amplitude) and σ (width of the Gaussian) are chosen to be: $\epsilon = 2.0$ and $\sigma = 0.4$. We set up a multidomain grid of $D = 10$ subdomains and we change the number of collocation points per subdomain to see how the error changes for both double precision and for 300-bit precision. We evolve the initial ‘‘perturbation’’ for the time corresponding to two bounces off the AdS boundary. Since we need very high accuracy, we have used a sixth-order Runge-Kutta 10,6(7) (see Refs. [44, 45] for details). This ODE solver uses ten intermediate steps to generate a sixth-order accurate in time integration with a seventh-order step that is used as an estimation of the error.

At any time step, we can compute the energy contained inside a sphere of a given compactified radius x , which is known as the mass function:

$$\mathcal{M}(t, x) = e^\delta \int_0^x dy e^{-\delta} \sin^2 y \left(\frac{U^2 + V^2}{2} \right), \quad (95)$$

so that the total energy contained in the spacetime is $M(t) = \mathcal{M}(t, \pi/2)$. According to the mathematical theory, $M(t)$ should not depend on time, it is a conserved quantity. Then, we can monitor the conservation of M as indicator of the accuracy of the simulation. To that end we introduce the following mass error function, defined as:

$$\Delta M(t) = \frac{|M(t) - M(t_o)|}{M(t_o)}. \quad (96)$$

We have performed a set of numerical evolutions to assess the relevance of arbitrary precision in these computations. In Figure 13 we show the evolution of the mass error function of Eq. (96). The purple line shows an evolution with a low number of collocation points ($N = 12$) and with double precision. The error oscillates in the range $10^{-12} - 10^{-11}$. Increasing the number of collocation points to $N = 18$ (red line in Figure 13) we can decrease the mass error down to around 10^{-14} . It is interesting to notice the different behaviour between these two lines. In the first case, there is plenty of oscillations and we estimate the error by taking the maximum value. This is due to the fact that here the error is determined by the discretization error in such a way that the total error can oscillate between the discretization and the round-off errors. In the second case we have reached by far the round-off error and the profile is quite flat. Then, it is obvious that it cannot be improved by using double precision. Just changing from double precision to 300-bit

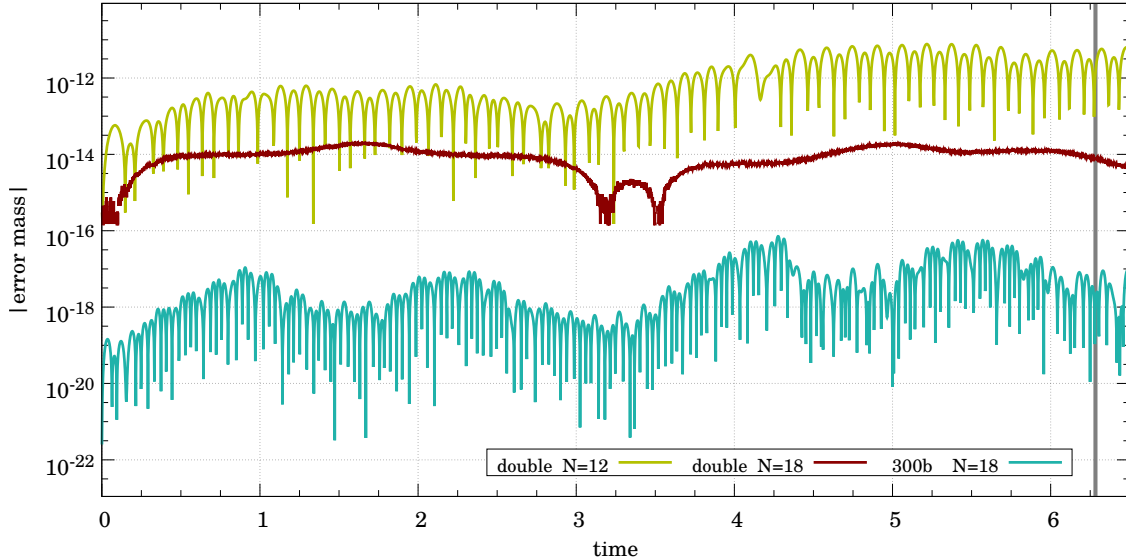


Figure 13: **Evolution of the Mass Error Function in AAdS Spacetimes.** We compare three different grid/precision configurations with $D = 10$ subdomains. Using double precision, the use of $N = 18$ collocation points per subdomain (red line) is enough to reach the round-off error. The same number of collocation points but with 300-bit precision (turquoise line) allows us to reduce a few orders of magnitude the error during the evolution. It is interesting to notice how, when the error is determined by the discretization error, several fluctuations are present while in the one dominated by machine round-off the error remains almost flat during the time evolution. The grey vertical line to the right shows the instant of time at which we measure the error for the study presented in Figure 14.

precision but with the same number of collocation points per subdomain, the error drops more than two orders of magnitude and, again, it is determined by the discretization.

Once the massless scalar field configuration has bounced twice off the AdS boundary and has come back to the initial location ($t \approx 2\pi$), we have studied not only the error mass function at that moment, but also the error in the characteristic fields U and V . To that end, we have used the absolute value of the last spectral coefficient in the subdomain where the error is maximum. This is shown in Figure 14 for domain configurations of $D = 10$ subdomains and for different number of collocation points and numerical precisions. As expected, the error in all the three quantities [ΔM (left plot), U (center plot), and V (right plot)] decays exponentially until we reach round-off error. For double precision (red points) this happens at values of the order of $\sim 10^{-14} - 10^{-15}$. This is easily improved when we used higher-order precision, like the one shown with turquoise dots in the same figure. This corresponds to 300-bit precision and allows to evolve the scalar field configuration with an accuracy below 10^{-24} with a number of collocation points per subdomain as small as $N = 28$, for a total of 290 collocation points.

5. Conclusions and Future Perspectives

In this paper we have shown the potential of the combination of Pseudo-Spectral Collocation methods and arbitrary-precision arithmetic for the solution of ordinary/partial differential equations, and more specifically for hyperbolic problems related to the description of gravitational collapse in relativistic gravitation. The exponential convergence of the PSC method makes it a very suitable choice for reaching the maximum accuracy associated with a certain bit precision with a relatively low number of discretization (collocation) points as compared with other techniques. In this sense, we have seen that the power-law convergence of finite difference algorithms makes it unfeasible to reach the needed accuracy within a reasonable number of discretization points. In addition, the PSC method does not require relevant changes in the algorithms as we increase the number of precision bits, in contrast with finite difference, where we need to adapt the algorithm so that the error scales in a way that we can reach the level of accuracy allowed by the choice of precision arithmetic.

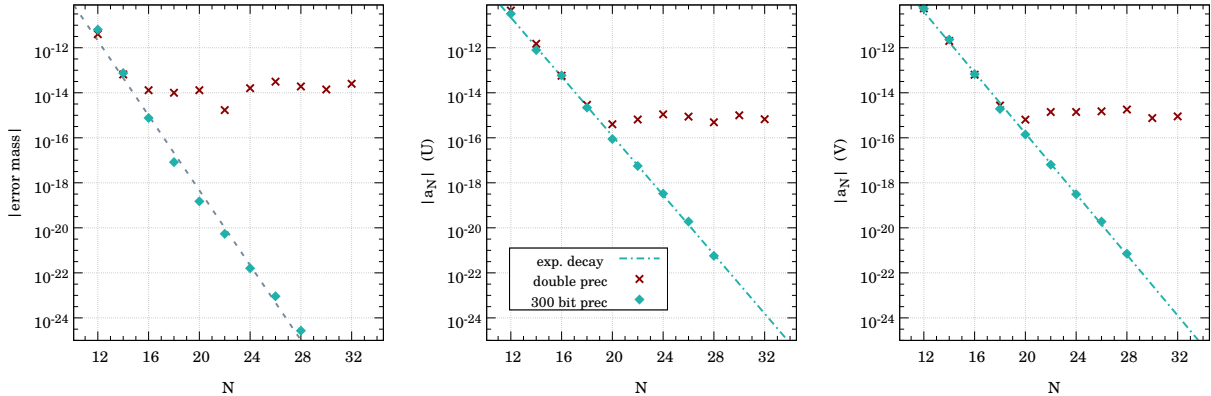


Figure 14: **Convergence of the Truncation Error in Evolutions in AdS Spacetimes.** The figure shows the error in an AdS spacetime evolution using double (red dots) and 300-bit (turquoise dots) precision computations. The plots represent the normalised mass error ΔM (left), the truncation error for U (centre), and the truncation error for V (right) with respect to the number of collocation points per subdomain. This information is measured at the same time ($t = 2\pi$) after the massless scalar field configuration has bounced twice off the AdS boundary. All the simulations use $D = 10$ subdomains.

In Sec. 3.3, we have seen that the main problem of arbitrary precision arithmetics is that it is usually implemented via a software layer that slows down significantly the computations with respect to the speed of standard double precision arithmetic. In this sense, the PSC method helps since the number of collocation points required is relatively small and therefore, they can be computationally demanding although the sparsity of the matrices involved in certain algorithms can be a drawback. Moreover, the multidomain scheme proposed in this paper allows for a simple parallelization of the computations, as we have shown with the use of OpenMP in our examples. We have also shown that the scalability of the multidomain scheme is close to the ideal case of full parallelism. Nevertheless, it would be desirable to explore improvements in the computation speed (and cost) based on an exploration of a more low-level approach to arbitrary precision arithmetic.

All the numerical examples and experiments reported in this paper have been carried out using a new library, the **ANETO** library [6], that we have developed out of our experience with the modelling of gravitational collapse in the context of General Relativity. Its current version has been released with a few basics tools to deal with evolution problems but it can be extended in the future to include other tools that PSC methods offer. In this sense, one of the main possible improvements would be to add a solver for linear ODEs and also the incorporation of tools for non-linear cases. Also some kind of Adapting Mesh Refinement method to allow the grid to be more flexible under different conditions or in a farther future the incorporation of higher dimensional problems. Another aspect that we have not discussed in this paper is time integration. As the demand for accuracy increases, this aspect becomes more and more important and then, high-order integration algorithms would be required both to respect the accuracy provided by the PSC method and arbitrary-precision arithmetics and also to reduce the number of steps in the evolution. For this reason, a spectral time integration like the one proposed in Refs. [46, 47, 36] can be an interesting solution to improve the accuracy of the evolutions with arbitrary precision arithmetic.

Acknowledgements

The authors acknowledge the high-performance computing resources provided by the Consorci de Serveis Universitaris de Catalunya (CSUC) and the Galicia Supercomputing Center (CESGA) under projects ICTS-CESGA-249 and ICTS-CESGA-266. They also acknowledge support from contracts ESP2013-47637-P, ESP2015-67234-P, and ESP2017-90084-P (Spanish Ministry of Economy and Competitiveness of Spain, MINECO). DS acknowledges support from a FPI doctoral contract BES-2012-057909 from MINECO.

Appendix A. The ANETO Library

The Arbitrary precision solvEr with pseudo-specTral MethOds (**ANETO**) library is a platform to use the PSC method to solve differential equations using arbitrary precision arithmetics. **ANETO** has been released as Free Software under a GNU General Public License (GPL) and it can be found in [6], including source code and full documentation of the classes and functions available as well as examples of its functionalities. The library was originally developed due to need to go beyond the standard double precision for the study of certain problems associated with gravitational collapse in the context of the General Theory of Relativity. We have used the library in this paper to show the great potential of combining the PSC method with arbitrary precision arithmetics.

The library has been developed using C++ templates, which allows for the use of any kind of data type. In several of the computations done for this paper, we have used standard types like **float** and **double** for single and double precision respectively. For the **quadruple precision** type we have used the `float128` type implemented in the Boost Multiprecision library [48]. For general bit precision, we have used the GNU's Multiple Precision Floating-Point Reliable (MPFR) Library [49], a C library for multiple-precision floating-point computations with correct rounding, with a C++ wrapper [50] as an interface.

The tools of the library are distributed in two different C++ classes following the structure described in Sec. 2. The first class is **spectral_grid<>** and generates an individual Lobatto-Chebyshev collocation grid. The second class is **multidomain<>** and generates a multidomain structure where each subdomain is a single Lobatto-Chebyshev collocation grid. In this appendix we briefly explain the main details of how these classes are implemented in the **ANETO** library.

Appendix A.1. Class Spectral Domain

The class **spectral_grid<>** generates a *Lobatto-Chebyshev* collocation grid defined on the *spectral* interval $X = [-1, 1]$ of $N + 1$ points [see Eq. (7) for the location of the collocation points]. We can then define functions on this interval which are fully characterized by their values at the collocations points of the grid, what we named as the *physical* representation of a function. In general, the information associated with any given function is stored using this representation but, quite frequently, some important operations are performed using the *spectral* representation, that is, the coefficients of the expansion in Chebyshev polynomials [see Eq. (8)]. The class **spectral_grid<>** makes the transformation between the two representations using a discrete cosine transformation (DCT). The library can carry out this transformation either through a matrix transformation, in that case the number of operations scales as $\sim N^2$, or using a Fast Fourier algorithm (FFT), in which case the number of operations scales as $\sim N \log N$. The FFT algorithm that the library used comes from the Eigen library [51], which is optimised for the case in which the number of points is a power of two and therefore, the recommended use (i.e. the default one), is to use the FFT in those cases and the matrix transformation in the rest.

This class can perform several types of operations on a Lobatto-Chebyshev grid, like for instance indefinite integrals. In that case, it distinguishes integration starting from the left boundary, $X_- = -1$, from integration starting from the right boundary, $X_+ = +1$. In the case of integration from the left, the operation is denoted by $I_L(X; \{f_i\}, I_-)$, where X is the any value in the spectral interval, $\{f_i\}$ ($i = 0, \dots, N$) are the collocation values of the integrand function and I_- is a boundary condition on the left boundary of the spectral integral. Then, the operation I_L returns the values at the collocation points of the accumulative integral compute from the left boundary, $X_- = -1$, given the boundary condition specified precisely by I_- . And the analogous operation can be introduced for indefinite integration from the right, which we denote by $I_R(X; \{f_i\}, I_+)$, where the only difference is that now we have to specify a boundary condition on the right boundary, $X_+ = 1$, that is, I_+ . The exact expressions and details are given in Eqs. (26) and (29) of Sec. 2.

One of the main advantages of the use of spectral methods is the accuracy that we have in the interpolation inside the spectral domain. In the **ANETO** library this is done in the spectral representation, which involves transforming back and forth from the physical representation [see Eq. (8)]. The class **spectral_grid<>** computes the value of the function on any point of the spectral domain. For efficiency purposes, once they are computed, the spectral coefficients are stored inside the class so they can be used afterwards to get values of the function on another location without recomputing them. This can be done, not only for the values of a given function, but also for its first and second derivatives. In the library, this is used to incorporate a very efficient and accurate root finding algorithm inside the class. It is implemented with an iterative Newton's method to find the root until the precision of the datatype used is

reached. If no root is present in the domain, the function will return the closest value, and if there is more than one, just one of them is returned.

Appendix A.2. Class Multidomain

The class `multidomain<>` generates a multidomain structure with the number of subdomains and collocation points per subdomain specified. The distribution of the subdomains can be chosen to be uniform or it can be fixed by specifying the location of their boundaries, which can be used to generate a mesh adapted to the resolution needs of the problem. The `multidomain<>` class manages the internal operations of the different subdomains and once it is created, its main features can be accessed without noticing the internal structure.

This class extends all the features present in the single domain class, increasing the functionalities in some aspects. For instance, the integration operations has the possibility of specifying the boundary condition on an arbitrary interior point, say x_C . Then, we can perform the integration according to the following expression

$$I_C(x) = I(x_C) + \int_{x_C}^x d\tilde{x} f(\tilde{x}). \quad (\text{A.1})$$

The `multidomain<>` class also provides the opportunity of using the dual-grid scheme according to the Eq. (43) of Sec. 2.1. This option allows us to significantly improve the accuracy in the computation of derivatives at the points near the subdomain boundaries.

For the root finding operation, two important cases have been added. One for monotonically increasing functions and another one for monotonically decreasing functions. In both of them, the root, if it exists, will be unique. If there is no root in the whole computational domain, the function will return an error code. For general functions, we can find the root indicating the subdomain where we expect it to be located and the library returns the closest value even in the case that there is no root in the subdomain.

References

References

- [1] D. H. Bailey, J. M. Borwein, High-Precision Arithmetic in Mathematical Physics, *Mathematics* 3 (2) (2015) 337. doi:10.3390/math3020337. URL <http://www.mdpi.com/2227-7390/3/2/337>
- [2] P. Grandclement, J. Novak, Spectral methods for numerical relativity, *Living Rev. Rel.* 12 (2009) 1. arXiv:0706.2286, doi:10.12942/lrr-2009-1.
- [3] C. Canuto, M. Y. Hussaini, A. Quarteroni, T. A. Zang, *Spectral methods: evolution to complex geometries and applications to fluid dynamics*, Springer Science & Business Media, 2007.
- [4] W. Bourke, *Spectral Methods in Global Climate and Weather Prediction Models*, Springer Netherlands, Dordrecht, 1988, pp. 169–220. doi:10.1007/978-94-009-3041-4_4. URL http://dx.doi.org/10.1007/978-94-009-3041-4_4
- [5] M. Ehrendorfer, *Spectral Numerical Weather Prediction Models, Other titles in applied mathematics*, Society for Industrial and Applied Mathematics, 2012.
- [6] D. Santos-Oliván and C. F. Sopena, ANETO library: Arbitrary precision solver with pseudo-spectral methods, <https://github.com/DSantos0/anetolib> (2017).
- [7] D. Santos-Oliván, C. F. Sopena, New Features of Gravitational Collapse in Anti-de Sitter Spacetimes, *Phys. Rev. Lett.* 116 (4) (2016) 041101. arXiv:1511.04344, doi:10.1103/PhysRevLett.116.041101.
- [8] D. Santos-Oliván, C. F. Sopena, Moving closer to the collapse of a massless scalar field in spherically symmetric anti-de Sitter spacetimes, *Phys. Rev. D* 93 (10) (2016) 104002. arXiv:1603.03613, doi:10.1103/PhysRevD.93.104002.
- [9] Sarmin, EN and Chudov, LA, On the stability of the numerical integration of systems of ordinary differential equations arising in the use of the straight line method, *USSR Computational Mathematics and Mathematical Physics* 3 (6) (1963) 1537–1543.
- [10] C. Canuto, M. Y. Hussaini, A. Quarteroni, T. A. Zang, *Spectral methods in Fluid Dynamics*, Springer-Verlag, 1988.
- [11] J. P. Boyd, *Chebyshev and Fourier Spectral Methods*, 2nd Edition, Dover, New York, 2001.
- [12] B. Fornberg, *A Practical Guide to Pseudospectral Methods*, Cambridge University Press, Cambridge, 1996.
- [13] B. Gustafsson, H.-O. Kreiss, J. Oliger, *Time dependent problems*, John Wiley & Sons, New York, 1995.
- [14] A. Bayliss, E. Turkel, Mappings and accuracy for chebyshev pseudo-spectral approximations, *Journal of Computational Physics* 101 (2) (1992) 349 – 359. doi:http://dx.doi.org/10.1016/0021-9991(92)90012-N. URL <http://www.sciencedirect.com/science/article/pii/002199919290012N>
- [15] D. Kosloff, H. Tal-Ezer, Modified chebyshev pseudospectral method with $o(n^{-1})$ time step restriction, *J. Comput. Phys.* 104 (1993) 457–469.
- [16] R. Peyret, *Spectral methods for incompressible viscous flow*, Vol. 148, Springer Science & Business Media, 2013.

- [17] R. Courant, D. Hilbert, *Methods of Mathematical Physics Volume II*, John Wiley and Sons, 1989.
- [18] W. H. Press, B. P. Flannery, S. A. Teukolsky, W. T. Vetterling, *Numerical Recipes: The Art of Scientific Computing*, Cambridge University Press, Cambridge (UK) and New York, 1992.
- [19] L. Dagum, R. Menon, OpenMP: an industry standard API for shared-memory programming, *Computational Science & Engineering*, IEEE 5 (1) (1998) 46–55.
- [20] M. Joldes, J.-M. Muller, V. Popescu, W. Tucker, CAMPARY: Cuda Multiple Precision Arithmetic Library and Applications, in: 5th International Congress on Mathematical Software (ICMS), Berlin, Germany, 2016.
URL <https://hal.archives-ouvertes.fr/hal-01312858>
- [21] C. Runge, Über empirische Funktionen und die Interpolation zwischen äquidistanten Ordinaten, *Zeitschrift für Mathematik und Physik* 46 (1901) 224–243.
- [22] J. Epperson, On the Runge example, *Amer. Math. Monthly* 94 (1987) 329–341. doi:10.2307/2323093.
- [23] S. W. Hawking, G. F. R. Ellis, *The Large scale structure of space-time*, Cambridge University Press, Cambridge, 1973.
- [24] C. W. Misner, K. Thorne, J. A. Wheeler, *Gravitation*, W. H. Freeman & Co., San Francisco, 1973.
- [25] R. M. Wald, *General Relativity*, The University of Chicago Press, Chicago, 1984.
- [26] E. Poisson, *A Relativist’s Toolkit. The Mathematics of Black-Hole Mechanics*, Cambridge University Press, Cambridge, 2004.
- [27] L. Lehner, Numerical relativity: A Review, *Class. Quant. Grav.* 18 (2001) R25–R86. arXiv:gr-qc/0106072, doi:10.1088/0264-9381/18/17/202.
- [28] M. Alcubierre, *Introduction to 3+1 numerical relativity*, International series of monographs on physics, Oxford Univ. Press, Oxford, 2008.
URL <https://cds.cern.ch/record/1138167>
- [29] E. Gourgoulhon, 3+1 Formalism and Bases of Numerical Relativity arXiv:gr-qc/0703035.
- [30] H. Stephani, D. Kramer, M. MacCallum, C. Hoenselaers, E. Herlt, *Exact solutions of Einstein’s field equations*, Cambridge University Press, Cambridge, 2003.
- [31] M. W. Choptuik, Universality and scaling in gravitational collapse of a massless scalar field, *Phys. Rev. Lett.* 70 (1993) 9–12. doi:10.1103/PhysRevLett.70.9.
- [32] B. Szilagyi, L. Lindblom, M. A. Scheel, Simulations of Binary Black Hole Mergers Using Spectral Methods, *Phys. Rev. D* 80 (2009) 124010. arXiv:0909.3557, doi:10.1103/PhysRevD.80.124010.
- [33] R. Haas, et al., Simulations of inspiraling and merging double neutron stars using the Spectral Einstein Code, *Phys. Rev. D* 93 (12) (2016) 124062. arXiv:1604.00782, doi:10.1103/PhysRevD.93.124062.
- [34] P. Canizares, C. F. Sopuerta, An Efficient Pseudospectral Method for the Computation of the Self-force on a Charged Particle: Circular Geodesics around a Schwarzschild Black Hole, *Phys. Rev. D* 79 (2009) 084020. arXiv:0903.0505, doi:10.1103/PhysRevD.79.084020.
- [35] P. Canizares, C. F. Sopuerta, J. L. Jaramillo, Pseudospectral Collocation Methods for the Computation of the Self-Force on a Charged Particle: Generic Orbits around a Schwarzschild Black Hole, *Phys. Rev. D* 82 (2010) 044023. arXiv:1006.3201, doi:10.1103/PhysRevD.82.044023.
- [36] R. Panosso, M. Ansorg, Axisymmetric fully spectral code for hyperbolic equations, *J. Comput. Phys.* 276 (2014) 357–379. arXiv:1402.7343, doi:10.1016/j.jcp.2014.07.040.
- [37] M. Oltean, C. F. Sopuerta, A. D. A. M. Spallicci, Particle-without-Particle: a practical pseudospectral collocation method for numerical differential equations with distributional sources arXiv:1802.03405.
- [38] C. Gundlach, Critical phenomena in gravitational collapse, *Phys. Rept.* 376 (2003) 339–405. arXiv:gr-qc/0210101, doi:10.1016/S0370-1573(02)00560-4.
- [39] C. Gundlach, J. M. Martin-Garcia, Critical phenomena in gravitational collapse, *Living Rev. Rel.* 10 (2007) 5. arXiv:0711.4620, doi:10.12942/lrr-2007-5.
- [40] D. Christodoulou, The Problem of a Selfgravitating Scalar Field, *Commun. Math. Phys.* 105 (1986) 337–361. doi:10.1007/BF01205930.
- [41] D. S. Goldwirth, T. Piran, Gravitational Collapse of Massless Scalar Field and Cosmic Censorship, *Phys. Rev. D* 36 (1987) 3575. doi:10.1103/PhysRevD.36.3575.
- [42] D. Garfinkle, Choptuik scaling in null coordinates, *Phys. Rev. D* 51 (1995) 5558–5561. arXiv:gr-qc/9412008, doi:10.1103/PhysRevD.51.5558.
- [43] P. Bizoń, A. Rostworowski, On weakly turbulent instability of Anti-de Sitter space, *Phys. Rev. Lett.* 107 (2011) 031102. arXiv:1104.3702, doi:10.1103/PhysRevLett.107.031102.
- [44] J. H. Verner, Explicit runge-kutta methods with estimates of the local truncation error, *SIAM Journal on Numerical Analysis* 15 (4) (1978) 772–790.
- [45] P. J. Prince, J. R. Dormand, High order embedded Runge-Kutta formulae, *Journal of Computational and Applied Mathematics* 7 (1) (1981) 67–75.
- [46] J. Hennig, M. Ansorg, A Fully Pseudospectral Scheme for Solving Singular Hyperbolic Equations on Conformally Compactified Space-Times, *J. Hyperbol. Diff. Equat.* 6 (2009) 161. arXiv:0801.1455, doi:10.1142/S0219891609001769.
- [47] J. Hennig, Fully pseudospectral time evolution and its application to 1+1 dimensional physical problems, *J. Comput. Phys.* 235 (2013) 322–333. arXiv:1204.4220, doi:10.1016/j.jcp.2012.10.040.
- [48] J. Maddock and C. Kormanyos, Boost Multiprecision Library, http://www.boost.org/doc/libs/1_66_0/libs/multiprecision/doc/html/index.html (2002).
- [49] L. Fousse, G. Hanrot, V. Lefèvre, P. Pélicier, P. Zimmermann, MPFR: A Multiple-precision Binary Floating-point Library with Correct Rounding, *ACM Trans. Math. Softw.* 33 (2). doi:10.1145/1236463.1236468.
URL <http://doi.acm.org/10.1145/1236463.1236468>
- [50] P. Holoborodko, MPFR C++, <http://www.holoborodko.com/pavel/mpfr/> (2008–2012).
- [51] G. Guennebaud, B. Jacob, et al., Eigen v3, <http://eigen.tuxfamily.org> (2010).